



The CMB on Large Angular Scales

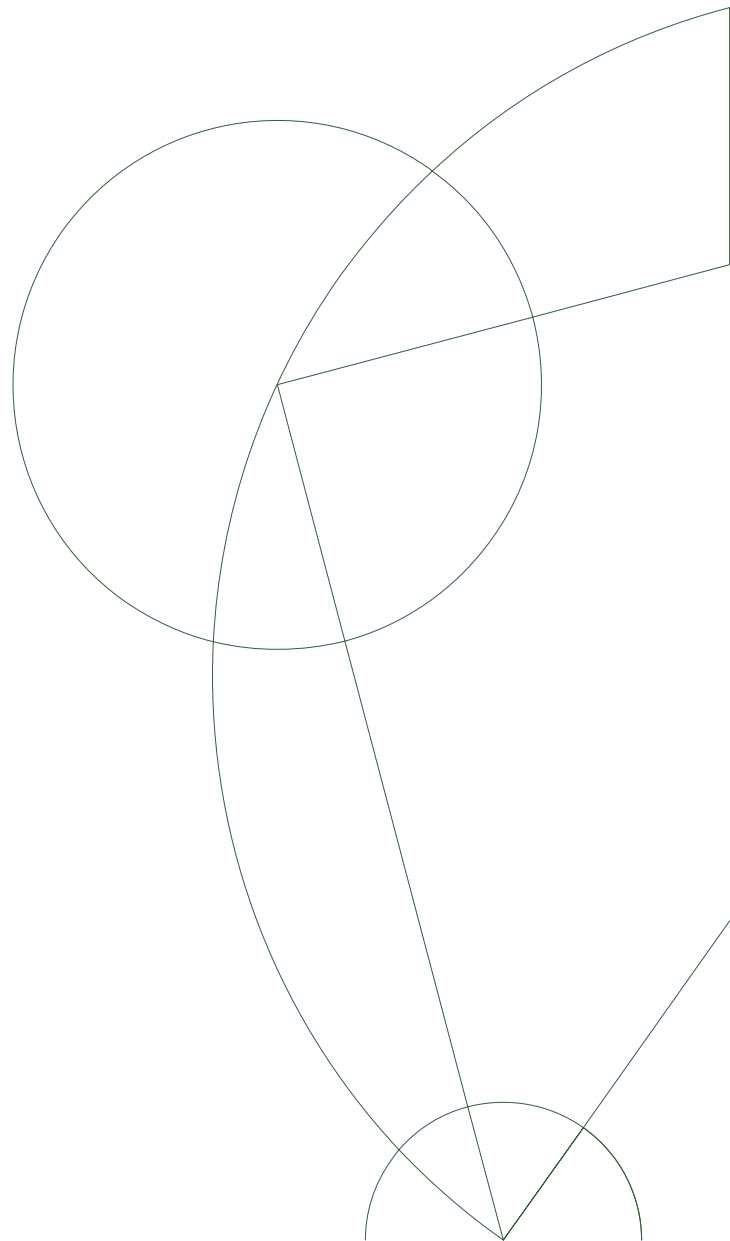
Master Thesis

Alexandra Zisimopoulou

Supervisor:

Pavel Naselsky
Niels Bohr Institute

July 24, 2020



Abstract

This thesis is dedicated to the description of the anomalies in the Cosmic Microwave Background (CMB) that have been observed on large angular scales and to the description of a theoretical framework that can possibly explain the nature of the dipolar power asymmetry observed in the CMB. Planck Collaboration of 2018, [9] confirmed several anomalies in the temperature map of the CMB on large angular scales, namely, the power asymmetry, the Cold Spot and other temperature peaks, the lack of large angle correlations and the point-parity asymmetry. Planck's mission searched for equivalent asymmetries in the polarization maps but the anomalies were not detected at a significant statistical level. Low signal-to-noise of the Planck's polarization data is a limiting factor and future, more sensitive observations are required to better investigate these anomalies. It is however intriguing to understand the origin of the anomalies in the temperature maps. It is suggested that the dipolar power asymmetry can be explained by the existence of an intrinsic CMB dipole. This temperature dipole is originated from superhorizon sized primordial isocurvature perturbations that existed in the axion field during inflation. The analysis was completed using MATLAB.

Acknowledgments

I would like to express my gratitude to my thesis supervisor Professor Pavel Nasselski of the Niels Bohr Institute at the University of Copenhagen, for giving me the opportunity to complete my thesis under his supervision. His comments helped me improve my thesis and have a better understanding of the physics related to this research.

I would also like to thank Dr. Mohamed Rameez. He inspired me to get involved with cosmology and read the academic research papers which are related to my thesis. He played a major part in organizing this thesis and he was present whenever I ran into a trouble or I had a question regarding my research.

Finally, I would like to thank my parents and friends who supported me throughout my years of study and through the process of writing this thesis.

Contents

Abstract	i
Acknowledgement	ii
1 Introduction	1
2 Large-Angle Anomalies in the CMB	3
2.1 Gaussianity and Isotropy	3
2.2 CMB Polarization	5
2.3 Stokes Parameters	9
2.4 Temperature and Polarization maps	12
2.5 Hemispherical Asymmetry: Excess of Power in one Hemisphere .	18
2.6 Hemispherical Asymmetry: Dipolar Modulation	18
2.6.1 Bipolar Spherical Harmonics	19
2.6.2 Dipole modulation: QML analysis	20
2.6.3 Variance Asymmetry	21
2.7 Cold Spot and Peaks	22
2.8 Point-parity asymmetry	23
2.9 Lack of Large Angle Correlations	25
3 The CMB Dipole Modulation	27
3.1 Kinematic Dipole	27
3.2 Superhorizon Perturbations	28
3.2.1 Adiabatic Perturbations	29
3.3 Intrinsic CMB Dipole	30
3.3.1 Generation of an Intrinsic Dipole	30
3.3.2 Dipole Modulation Amplitude	32
3.4 Parameter Estimation	36
4 Conclusion	40
Appendices	42
A SI Condition in Harmonic Space	43
Bibliography	44

Chapter 1

Introduction

The model of the Universe that is mostly accepted is based on two Dark Components: the Dark Matter and the Dark Energy, which both present a big challenge for physicists, since their origin is unknown. The Dark Matter paradigm initiate an intensive theoretical and experimental investigations of the possible candidates beyond Particle Standard Model. The origin of Dark Energy phenomena is still unknown, which generates intensive theoretical and experimental investigations in a framework of forthcoming ESA Euclid project.

In addition to these fundamental problems of modern physics, it is necessary to note several important astrophysical problems that are actively discussed in modern literature. The first of them is emerging the trend in the differences between local measurements of the Hubble constant, [52] and its determination from the Planck data and Baryonic Acoustic Oscillations, [8], [19].

Needless to mention that the Hubble constant cannot be measured from CMB temperature anisotropy data directly due to the well known degeneracy, [42]. The global determination of the Hubble constant using the Planck data is slightly lower with respect to the local value H_0 , [13]. It is not clear what is the origin of this tension and theoretical study is underway.

At the same time, WMAP [63], Planck 2013, 2015 and 2018 temperature sky maps [7], [6], [9] detected several anomalies, understanding the origin of which is important for the design of a realistic model of the modern Universe. The most significant of them are: the the power asymmetry [55], [35], the Cold Spot [7],[5],[55] and the Parity asymmetry [55],[7]. The first discovery of the Cold Spot was in the WMAP first-year data, [63]. All these anomalies can be modelled through implementation of weak statistics anisotropy of the primordial perturbations, [5]. An other project analyzing the CMB sky that we need to mention, is ACT (Atacama Cosmology Telescope) with several completed missions, such as the recent measurement of the CMB power spectra, [21].

In this work, we will describe the anomalies in the temperature sky maps that have been confirmed by the Planck 2018 release [9] and observed by other missions [63], [7], [6]. We will also investigate whether these anomalies are also observed in the polarization data as Planck 2018 mission has already described, [9]. Finally we will consider the dipole power asymmetry observed in the CMB

and try to explain the nature of this anomaly with the presence of an intrinsic CMB dipole related to superhorizon sized primordial isocurvature perturbations that existed on inflation together with adiabatic perturbations.

The outline of my thesis is the following:

Chapter 2 is devoted to the description of several anomalous features observed in the CMB sky using temperature and polarization maps of Planck 2015 and 2018 data, [6], [9]. A simplified description of the theoretical framework of polarization related to the CMB is given.

Chapter 3 is devoted to the existence of an intrinsic CMB dipole. In addition to the kinematic dipole, intrinsic fluctuations to the CMB can arise to compensate the axion energy density fluctuation. This perturbation is called superhorizon-sized isocurvature due to the fact that during inflation, the energy density contained in the axion field is negligible leading to insignificant curvature fluctuations, [61]. This mode could explain the origin of the large signal of the dipole modulation amplitude observed in the lower multipoles $l \leq 64$, as noted in [6].

In Conclusion we summarize the aforementioned and describe perspectives for future investigation as well as a planned observatory, the LiteBIRD, which aims to study the B-mode polarization of the CMB.

Chapter 2

Large-Angle Anomalies in the CMB

The Planck 2015 and 2018 data [6],[9] confirm a number of anomalies in the CMB temperature on large angular scales. At the same time CMB polarization maps can reveal anomalies in the CMB and if these are related to any existing anomalies in the CMB temperature field. A comparison between the two maps (polarization map or temperature field) could also reveal in one map statistically significant anomalies that are unrelated to an existing feature of the other map. If this is true, it is challenging to explain the origin of the signal. The study of the polarization of the CMB can unravel more information about the nature of the temperature fluctuations and at the same time test several cosmological models.

The temperature fluctuations are classified as scalar, vectors and tensor depending on their transformation properties under rotations, [39]. These fluctuations give rise to different patterns in the polarization field whether it is its intrinsic structure or its correlation with the temperature fluctuations. As a result polarization can help us distinguish the sources of anisotropy.

Linear polarization of the CMB is generated from the Thomson scattering of quadrupolar temperature anisotropies on the last scattering surface. It can be decomposed into a gradient (E-modes) and a curl component (B-modes). Scalar i.e. density perturbations produce only E-modes, while tensor perturbations i.e. gravitational waves, produce both E- and B-modes, [39].

2.1 Gaussianity and Isotropy

As stated in Planck 2018 analysis, [9], an N-point correlation function is defined as the average products of N observables, measured in a fixed relative orientation on the sky

$$C_N(\theta_1, \dots, \theta_{2N-3}) = \langle X(\hat{n}_1) \dots X(\hat{n}_N) \rangle \quad 2.1$$

where the unit vectors $\hat{n}_1, \dots, \hat{n}_N$ span an N-point polygon and the bracket denotes the ensemble average, that is an average over all possible configurations of the field. In Planck 2018 analysis, [9] the quantity X corresponds whether to the temperature of the CMB T , or to one of the Stokes parameters Q and

U describing the linearly polarized radiation in direction \hat{n} , as we will discuss later in this text.

For statistically isotropic field the N-point correlation function does not depend on the position or orientation of the N-point polygon on the sky. However it depends on the shape and size of the polygon, [9].

The temperature anisotropies of the CMB are described by a scalar random field, [33],[34]

$$\Delta T(\hat{n}) = T(\hat{n}) - T_0 \quad 2.2$$

on a 2-dimensional surface of a sphere, the surface of last scattering. $\hat{n} = (\theta, \phi)$ is a unit vector on the sphere and $T_0 = \int \frac{d\Omega_{\hat{n}}}{4\pi} T(\hat{n})$ represents the mean temperature of the CMB, $T_0 = 2.7255K$, [57].

In Gaussian fields, the two-point correlation function

$$C(\hat{n}, \hat{n}') = \langle \Delta T(\hat{n}) \Delta T(\hat{n}') \rangle \quad 2.3$$

contains all the statistical information encoded in the field. The CMB anisotropy is predicted and observed to be consistent with a Gaussian random field, [6], [9].

We can expand the temperature anisotropy field into spherical harmonics as, [33]

$$T(\hat{n}) = \sum_{l,m} a_{l,m}^T Y_{l,m}(\hat{n}) \quad 2.4$$

where the complex quantities, $a_{l,m}$ are given by,

$$a_{l,m}^T = \int d\Omega_{\hat{n}} Y_{lm}^*(\hat{n}) T(\hat{n}) \quad 2.5$$

For a Gaussian CMB anisotropy, $a_{l,m}^T$ are Gaussian random variables and thus, the covariance matrix $\langle a_{l,m}^T a_{l',m'}^{T*} \rangle$ fully describes the whole field, [33]. When studying the CMB anisotropy, the $l = 0$ term is the monopole anisotropy corresponding to a homogeneous and isotropic signal, the $l = 1$ is the dipole anisotropy, the $l = 2$ is the quadrupole anisotropy, ect.

A random field $\Phi(\mathbf{r})$ is statistically homogeneous if under the coordinate transformation $\mathbf{r} \rightarrow \mathbf{r} + \delta\mathbf{r}$, [33]

$$\begin{aligned} \langle \Phi(\mathbf{r}) \rangle &= \langle \Phi(\mathbf{r} + \delta\mathbf{r}) \rangle \\ C_{\Phi}(\mathbf{r}_1, \mathbf{r}_2) &= C_{\Phi}(\mathbf{r}_1 + \delta\mathbf{r}, \mathbf{r}_2 + \delta\mathbf{r}) \end{aligned} \quad 2.6$$

Statistical isotropic fields are statistical homogeneous fields which depend only on the magnitude and not the direction of the vector $\mathbf{r} = \mathbf{r}_2 - \mathbf{r}_1$. This means that,

$$C_{\Phi}(\mathbf{r}) = C_{\Phi}(r), \quad r = |\mathbf{r}| = \sqrt{\mathbf{r} \cdot \mathbf{r}} \quad 2.7$$

Notice that, the covariance, $C_{\Phi}(\mathbf{r}_1, \mathbf{r}_2)$, of a statistically homogeneous field depends only on the difference $\mathbf{r}_1 - \mathbf{r}_2$ if we set $\delta\mathbf{r} = -\mathbf{r}_1$ in the second equation of

2.6. For a Gaussian statistical isotropic field the covariance matrix is diagonal, [33], Appendix A

$$\langle a_{lm}^T a_{l'm'}^{T*} \rangle = C_l^{TT} \delta_{ll'} \delta_{mm'} \quad 2.8$$

where C_l is the angular power spectrum of CMB anisotropy and it encodes all the information of the field.

2.2 CMB Polarization

On the last scattering surface, the primordial photons re-scatter through Thomson scattering generating a linear polarization pattern on the sky. The Thomson scattering cross section depends on polarization as, [39]

$$\frac{d\sigma_T}{d\Omega} \propto |\hat{\varepsilon} \cdot \hat{\varepsilon}'|^2 \quad 2.9$$

where $\hat{\varepsilon}$ and $\hat{\varepsilon}'$ are the incident and the scattered polarization directions respectively.

To put in another words, an electron will oscillate by an incoming plane wave of radiation in the direction of the electric field vector \mathbf{E} . The polarization state that is parallel to the direction of propagation of the incident direction does not pass through. The scattered radiation has polarization parallel to the incident polarization and its intensity peaks in the direction normal to the incident polarization, [39],[51]. At the same time the frequency of the photon does not change before and after the scattering process.

In the case where the incident radiation is isotropic (monopole) the outgoing radiation remains unpolarized. If we have two incident waves like in Figure 2.1 and the radiation is isotropic, the outgoing radiation along the x and y axis will have equal intensities leading to unpolarized light. This is due to the fact that orthogonal polarization states coming from different incident directions are separated by 90° balancing each other so the outgoing radiation remains unpolarized, [39],[51].

For example in Figure 2.1 the outgoing wave is in the \hat{z} direction while the incoming radiation is in \hat{x} and \hat{y} axis. Through Thomson scattering described above the intensity of the x component of the outgoing radiation comes from the radiation incident from the \hat{y} direction, while the y component of the outgoing ray comes from the radiation incident from the \hat{x} direction. Since we are discussing about isotropic radiation the incoming amplitudes are the same and thus the outgoing wave is unpolarized. The outgoing radiation resulting from incident dipole radiation is also unpolarized, [51].

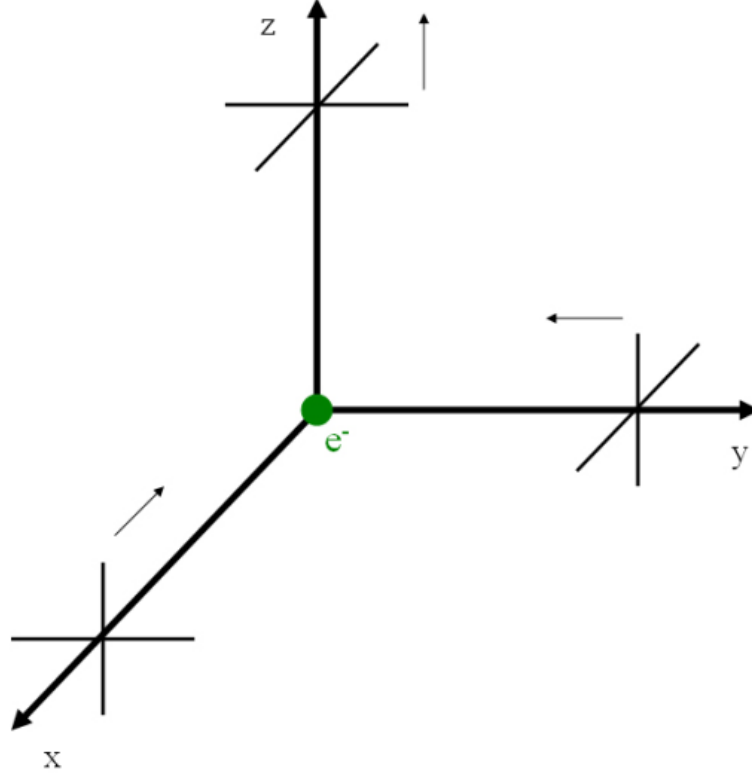


Figure 2.1: Thomson scattering of incoming isotropic radiation. The outgoing ray is unpolarized. This image was adapted from, [51].

Polarization of the scattered radiation can be produced when the incident radiation field has a quadrupolar variation in intensity or temperature, whose intensity peaks are separated consecutively by $\pi/2$, [39].

Thomson scattering of radiation with a quadrupole anisotropy is depicted in Figure 2.2. The blue thick and the red thin lines indicate the hot and cold radiation comparing to the average, respectively. More specific, the intensity of the outgoing radiation is greater along the y axis than along x axis. As a result the outgoing radiation is polarized, [51].

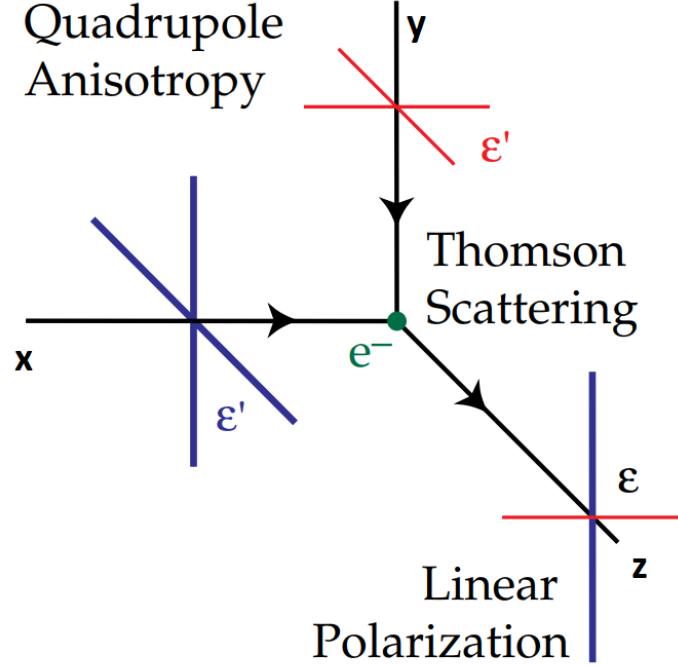


Figure 2.2: Thomson scattering of radiation when a quadrupole anisotropy generates linear polarization. The picture was adapted from [39].

In the multipole decomposition of the radiation field into spherical harmonics, $Y_{lm}(\theta, \phi)$ the quadrupole moments are represented by $l = 2$, $m = 0, \pm 1, \pm 2$. The temperature fluctuations can be distinguished to three categories: scalar (compressional), vector (vortical) and tensor (gravitational wave) perturbations. Each of these perturbations produce a different pattern in the polarization. This means that investigating the pattern of polarization can reveal information about the generation mechanism for fluctuations in the early universe, [39]. The scalar, vector, and tensor quadrupole anisotropy correspond to $m = 0, \pm 1, \pm 2$, respectively.

Polarization in the CMB can be generated by a quadrupole anisotropy of the photon flux at one point on the last scattering surface, when the universe is still ionized, [51]. Before recombination the mean free path of photons is too small, since the photons are scattered by Thomson scattering rapidly and the outgoing photons have random directions destroying any quadrupole anisotropy and polarization, [39], [45]. The photons and the electrons stay coupled in thermal equilibrium.

When the temperature of the Universe drops down to 0.1eV , electron and protons begin to create neutral hydrogen atoms and the radiation decouples. A quadrupole is produced at times near decoupling before the electron density

becomes too small and as soon as the photons are free streaming, [45].

In general, density perturbations create temperature fluctuations. Overdense regions are effectively cold initially, [39]. On small scales flows are established from hot temperature regions to cold effective temperature regions. As stated in [64]: Velocity gradients in the photon-baryon fluid lead to a quadrupole component of the intensity distribution, which, through Thomson scattering, is converted into polarization.

At first we will consider an observer located in a trough of a plane wave, the red region in Figure 2.3, [39]. The velocity of the flow \mathbf{v} is $\mathbf{v} \parallel \mathbf{k}$, while $\nabla \times \mathbf{v} = 0$. The observer sees a quadrupole with a moment $m = 0$, since hot photons from the peaks move in the middle from the $\pm \hat{k}$ directions. At the top the opposite effect occurs while $m = 0$. The result is a quadrupole with $m = 0$, [39]. The quadrupole moment $m = 0$ will define the corresponding polarization pattern produced from Thomson scattering.

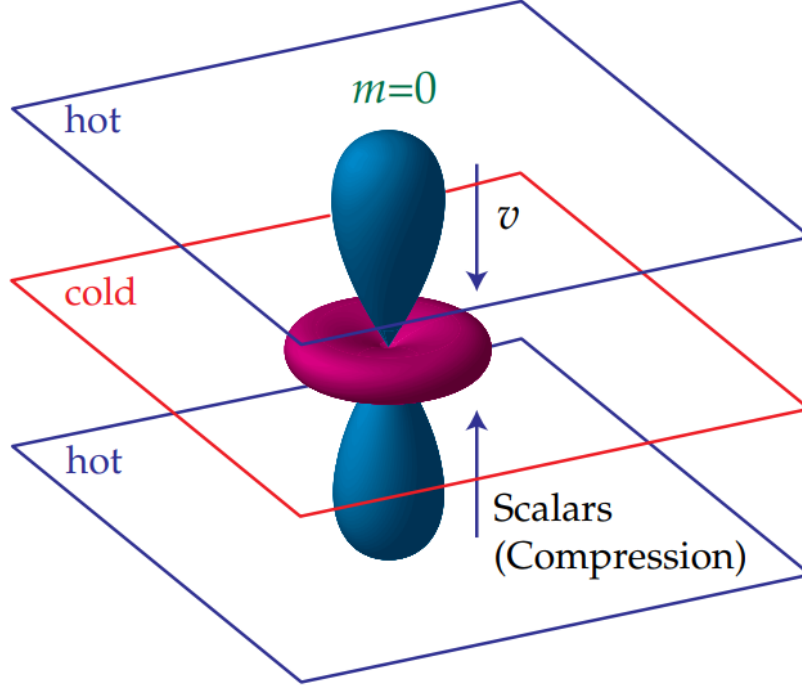


Figure 2.3: The scalar quadrupole moment, $l = 2$, $m = 0$. The Figure was adapted from [39].

Vector perturbations get damped by expansion and only the scalar and tensor ones survive, [43]. Tensor fluctuations are traceless perturbations to the metric, or equivalently, gravitational waves, [39]. As before, Thomson scattering transforms the quadrupole temperature anisotropy related to the tensor

perturbations into a local polarization field in a distinguish pattern.

Moreover, inflation produces coherent acoustic oscillations in the early Universe. Acoustic peaks in the temperature power spectrum represent density extrema and polarization peaks represent velocity extrema, [45]. For coherent oscillations these maxima are located in the same range of angular scales, see Figure 2.4. This is an example of a possible measurable signal of the CMB.

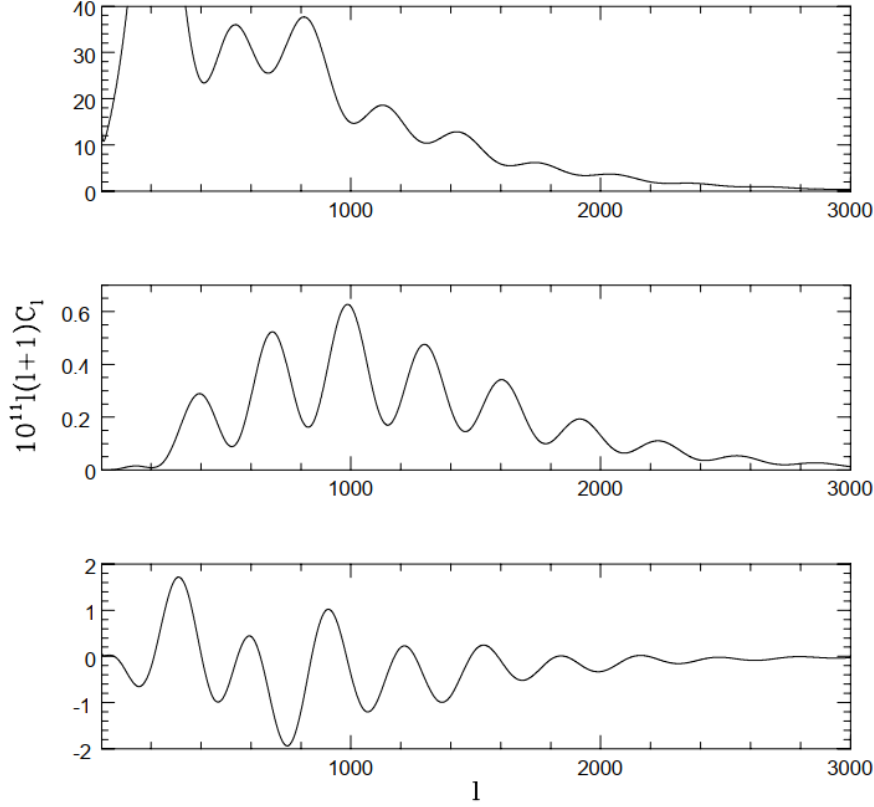


Figure 2.4: The power spectra for temperature fluctuations (top), polarization (center) and temperature-polarization correlation (bottom) for a typical inflationary model. The oscillations remain in phase up to $l = 3000$. The picture was adapted from, [45]

2.3 Stokes Parameters

In order to analyse the polarization data from Planck 2018, [9] they used scalar quantities, which remain invariant under coordinate transformations, defined by a combination of the Stokes parameters Q and U, which measure the linear po-

larization. An invariant quantity that was used is the square of the polarization amplitude P^2 , where, [9]

$$\begin{aligned}\mathbf{P} &= \sqrt{Q^2 + U^2} \hat{\phi} \\ \phi &= \frac{1}{2} \tan^{-1} \frac{U}{Q}\end{aligned}\tag{2.10}$$

where ϕ is the polarization angle and $\hat{\phi}$ the unit vector in the direction of the polarization.

The Stokes parameters depend on the reference frame. If the reference frame \hat{n}_{ref} is rotated by an angle θ around \hat{n} , then Q and U rotate to Q_r and U_r by an angle 2θ as

$$(Q_r \pm iU_r)(\hat{n}) = e^{\mp 2i\theta} (Q \pm iU)(\hat{n})\tag{2.11}$$

The quantities $Q \pm iU$ transform as spin 2-variables under rotations around the \hat{n} axis. [48] Therefore they can be expanded by the spin-2 spherical harmonics, [48]

$$(Q \pm iU)(\hat{n}) = \sum_{l=2}^{\infty} \sum_{m=-l}^l a_{lm}^{(\pm 2)} {}_{\pm 2}Y_{lm}(\hat{n})\tag{2.12}$$

where ${}_{\pm 2}Y_{lm}(\hat{n})$ are the spin-weighted spherical harmonics and $a_{lm}^{(\pm 2)}$ are the corresponding harmonic coefficients.

The scalar quantities referred to as E and B modes are commonly used for the global analysis of CMB data. These real scalar quantities have opposite behaviour under parity, [9]

$$\begin{aligned}E(\hat{n}) &= \sum_{l=2}^{\infty} \sum_{m=-l}^l a_{lm}^E Y_{lm}(\hat{n}) \\ B(\hat{n}) &= \sum_{l=2}^{\infty} \sum_{m=-l}^l a_{lm}^B Y_{lm}(\hat{n})\end{aligned}\tag{2.13}$$

where

$$\begin{aligned}a_{lm}^E &:= \frac{-1}{2} \left(a_{lm}^{(2)} + a_{lm}^{(-2)} \right) \\ a_{lm}^B &:= \frac{i}{2} \left(a_{lm}^{(2)} - a_{lm}^{(-2)} \right)\end{aligned}\tag{2.14}$$

The harmonics of an E-mode have $(-1)^l$ (positive) parity on the sphere, while the harmonics of a B-mode have $(-1)^{l+1}$ (negative) parity, [39]. Under the following transformation, $\hat{n} \rightarrow -\hat{n}$ the E-mode remains unchanged for even l , while the B-mode changes sign. Figure 2.5 illustrates this process for $l = 2$ and $m = 0$. Also Figure 2.6 illustrates some typical polarization patterns.

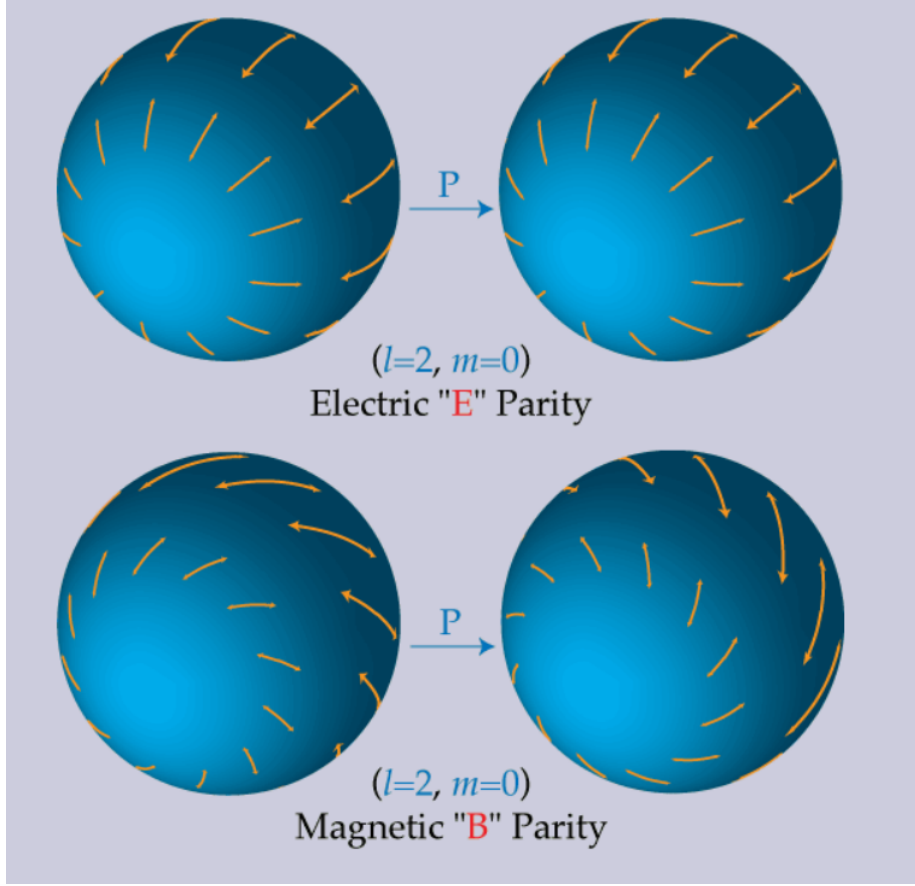


Figure 2.5: The behaviour of the E-mode and B-mode under a parity transformation, here $l = 2, m = 0$. even and odd respectively. The Figure was adapted from [4].

The temperature and polarization anisotropy patterns are correlated, [39]. Under the condition of statistical isotropy the correlation between correlations between T, E and B modes is written as, [51], [45]

$$\begin{aligned}
 \langle a_{lm}^T a_{lm}^{E*} \rangle &= \delta_{ll'} \delta_{mm'} C_l^{TE} \\
 \langle a_{lm}^E a_{lm}^{E*} \rangle &= \delta_{ll'} \delta_{mm'} C_l^{EE} \\
 \langle a_{lm}^B a_{lm}^{B*} \rangle &= \delta_{ll'} \delta_{mm'} C_l^{BB} \\
 \langle a_{lm}^B a_{lm}^{E*} \rangle &= \langle a_{lm}^B a_{lm}^{T*} \rangle = 0
 \end{aligned}
 \tag{2.15}$$

where C^{TE}, C^{EE}, C^{BB} are the corresponding power spectra. The correlations of BT and BE vanish because the B mode changes sign under parity transformation, [51], [45].

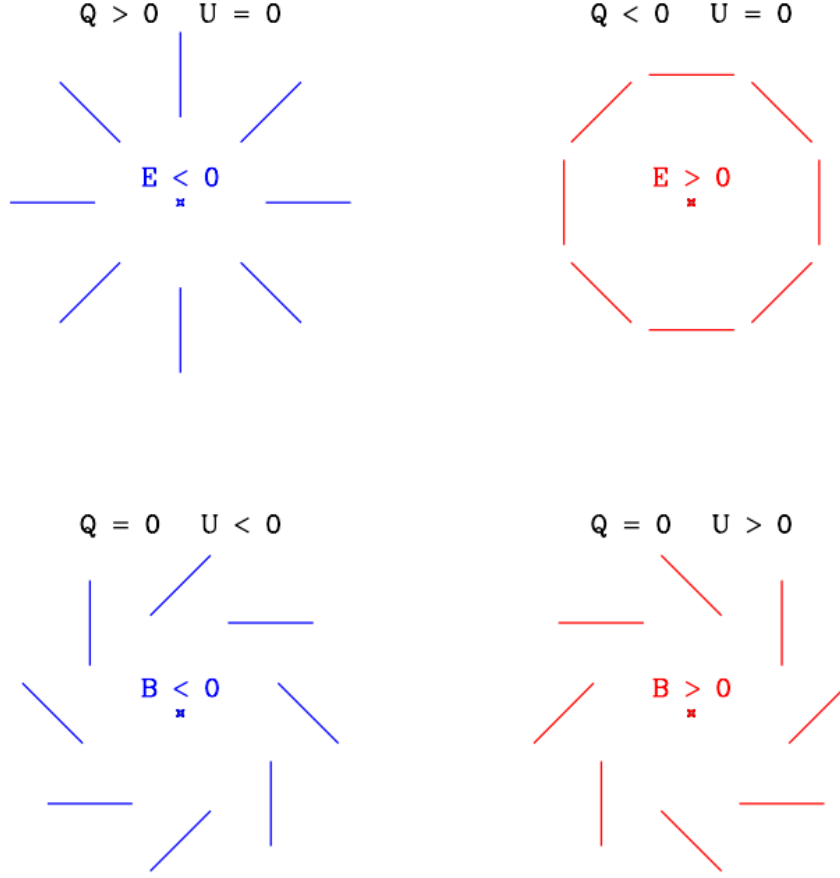


Figure 2.6: Typical E or B type polarization patterns. The Figure was adapted from [64].

CMB polarization can allow us to separate scalar perturbations from tensor perturbations, [64]. As stated in [43] scalar perturbations only generate positive parity polarization patterns, and therefore can only produce E- modes CMB polarization fluctuations. On the other hand, tensor perturbations can produce both E and B Polarization: tensor fluctuations. On the contrary, tensor fluctuation can produce both E- and B- modes of polarization.

2.4 Temperature and Polarization maps

WMAP [25] and Planck temperature sky maps [6], [9] aimed to understand the nature of the cosmic microwave background by studying the temperature fluctuations. In the following sections we will describe some of the anomalies of

the CMB they analyzed.

Figure 2.7 represents a map of the CMB temperature fluctuations as observed by ESA's Planck satellite, [3] and filtered on large angular scales, around 5° and larger. The u-shaped curve in the figure separates the northern hemisphere (central region) from the southern hemisphere. As we will discuss later in this text there is an excess of power in one hemisphere. The black circle represent the Cold Spot, that is a low temperature spot. Comparing the signal and noise map with the map containing only the signal, no anomalies can be found in the noise map, for example the Cold Spot. This means that the anomalies are not fake.

At the same time Planck 2018 release [9] looked for the equivalent anomalies in the polarization maps. Figure 2.8 illustrates the CMB polarization amplitude of the fluctuations filtered again on large angular scales, around 5° and larger. However Planck's observations did not show any anomalies at a statistically significant level. According to [9] and [2] the two maps in Figure 2.8 indicate possible anomalies, for example a power asymmetry between the two hemispheres. However, they are statistically insignificant.

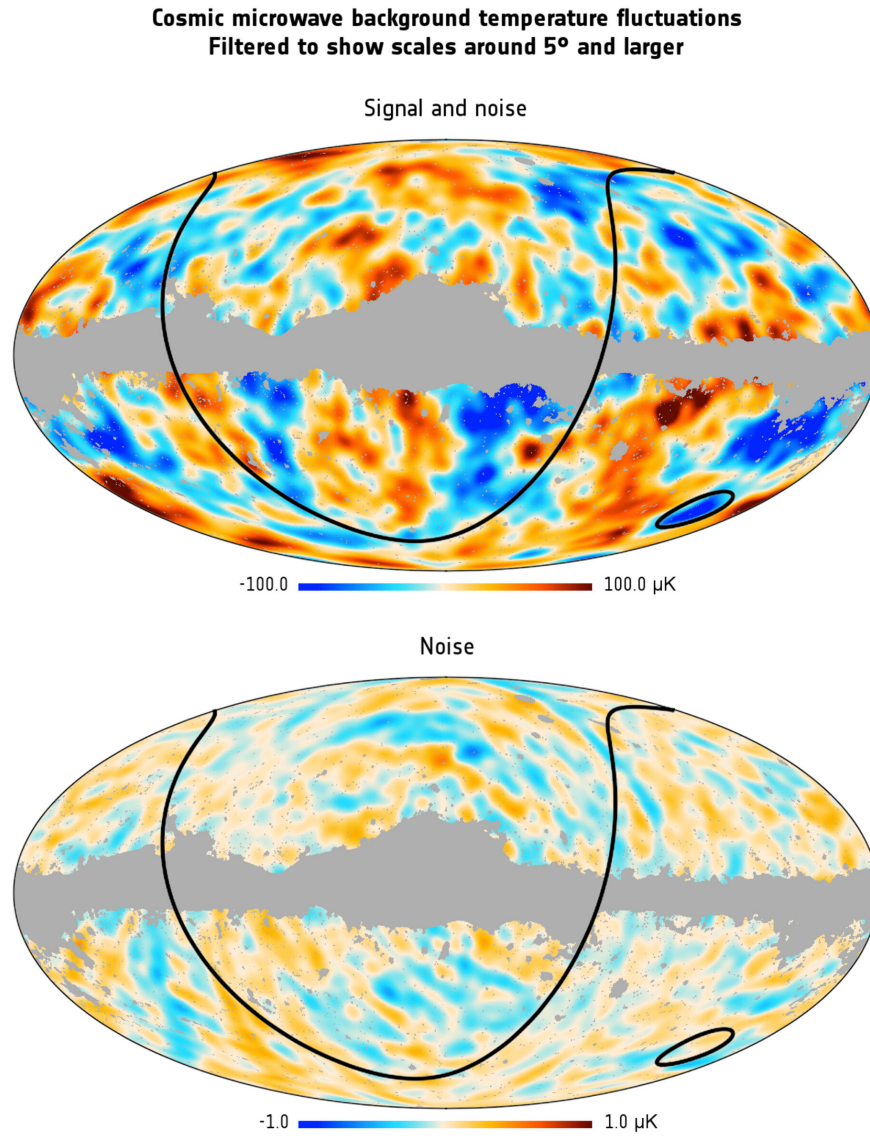


Figure 2.7: This Figure was adapted from ESA and the Planck Collaboration, [3].

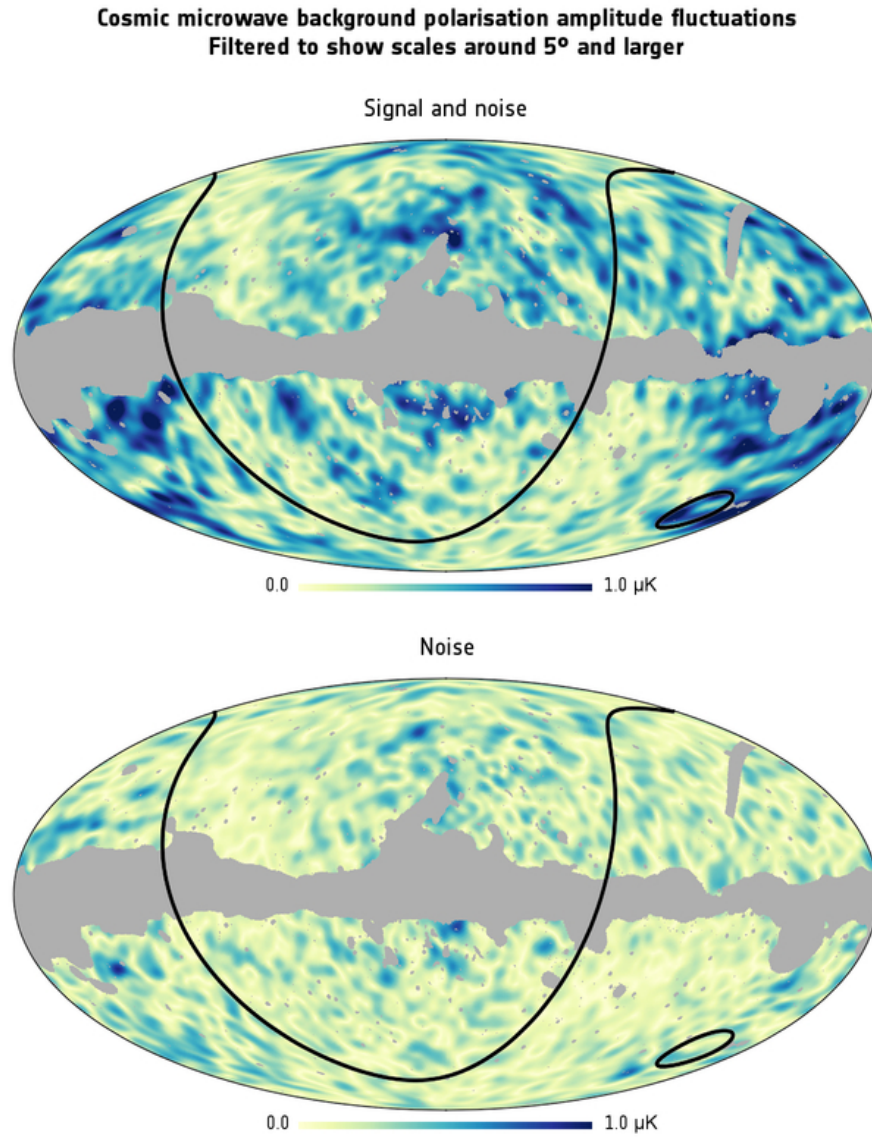


Figure 2.8: This Figure was adapted from ESA and the Planck Collaboration, [2].

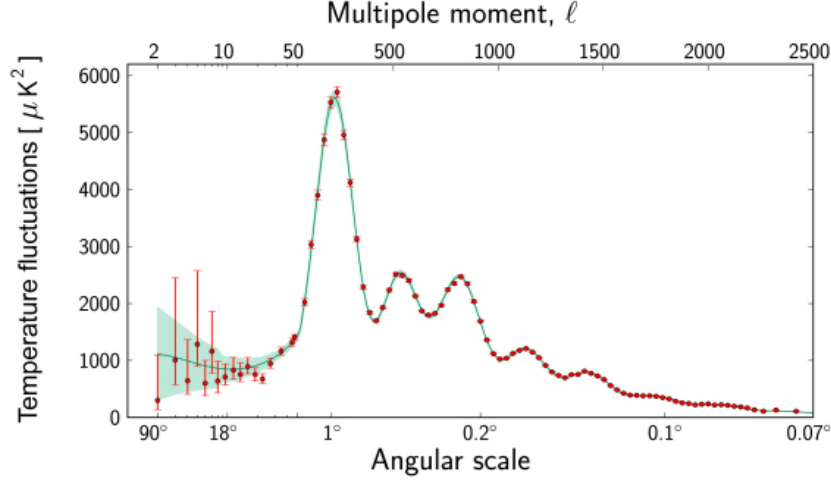


Figure 2.9: Power spectrum of temperature fluctuations in the Cosmic Microwave Background. This Figure was adapted from ESA and the Planck Collaboration, [1].

Figure 2.9 shows the power spectrum of temperature fluctuations in the CMB. The larger angular scales (low multipoles) are located on the left hand side in the figure while the smallest (large multipoles) on the right hand side. The red spots correspond to the measurements. The error bars correspond to measurement errors and the cosmic variance. The green line represents the best fit of the standard model of cosmology to the Planck data, while the shadowed region corresponds to other models that fit the data, [7].

In this Figure 2.9 too, some anomalies can be observed. On large angular scales, between 90° and 6° , the predictions of the best fit model are about 10% weaker compared to the observations. Also, there is one observation for angular scales larger than 6° that does not fit to the cosmological models, [7].

Figure 2.10 illustrates the CMB angular power spectra measurements from several missions and for the TT , TE , EE , and BB correlations. The image was adopted from [26]. Notice that not a lot of missions have studied the B-mode polarization. As we will discuss in Conclusion LiteBIRD, [41] is a promising mission which aims to study the B-mode polarization.

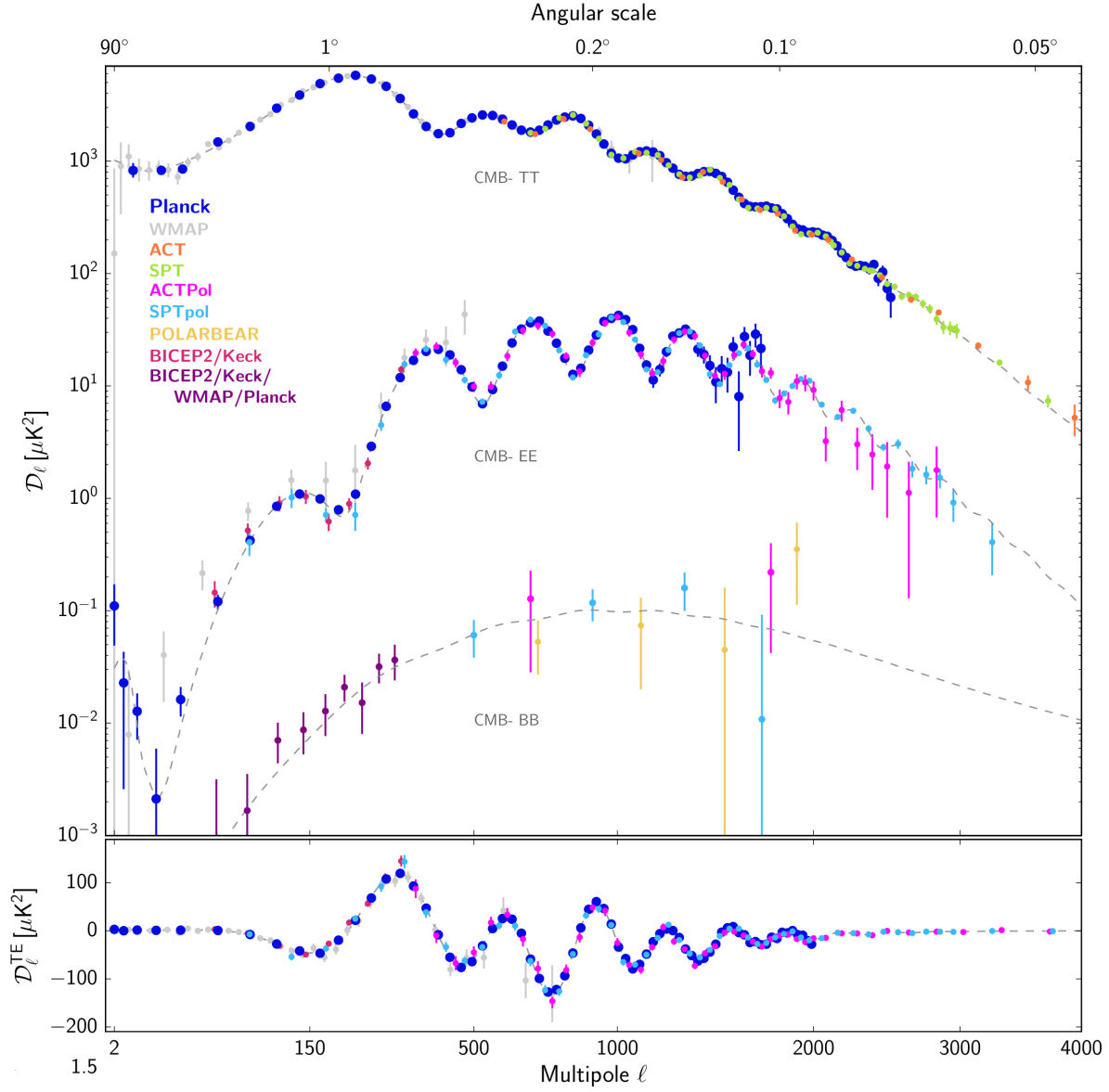


Figure 2.10: Power spectra measurements from several missions and for the TT , TE , EE , and BB correlations [26].

In the next sections we will discuss some of the anomalies using not only the CMB temperature sky maps but also the polarization data, relative to Planck 2015 and 2018 releases [6], [9].

2.5 Hemispherical Asymmetry: Excess of Power in one Hemisphere

The hemispherical power asymmetry includes whether an excess of power in one hemisphere or a directional dependence of the CMB angular power spectrum. We will first discuss the excess of power in one hemisphere and afterwards the dipolar power asymmetry, [9]

Several temperature sky maps have reported an asymmetry between the real-space N-point correlation functions computed on hemispheres [24],[6]. More specific Planck 2015 data tested the asymmetry using three different frames, the ecliptic coordinate frame, corresponding to the hemispheres separated by the ecliptic equator, the frame defined by the dipole modulation (DM) and the frame where the hemispheres are determined by the Doppler boost (DB).

The largest asymmetry was observed in ecliptic coordinates while a notable also asymmetry existed in the DM frame. In the DB frame Planck 2015 data, [6] did not find any significant asymmetry.

An asymmetry in the polarization field was tested by the Planck 2018 data, [9], where they used the ecliptic and the DM reference frames. The DM reference frame is divided into the positive and the negative hemisphere depending on the sign of the DM amplitude, [9]. The DM direction adopted in the Planck 2018 analysis $(l, b) = (221^\circ, -20^\circ)$ corresponds to the positive hemisphere. In order to find an asymmetry they used 2-point and 3-point correlation functions of several possible permutations of the T, Q, and U maps. The analysis in the DM reference frame showed a somewhat significant asymmetry in the negative hemisphere.

2.6 Hemispherical Asymmetry: Dipolar Modulation

Planck 2018 data analysis confirmed the isotropy violation on large angular scales related to the dipolar temperature asymmetry that has been observed previously in the WMAP [25] and Planck 2015, [6] releases. At the same time Planck Collaboration tried to find an equivalent asymmetry in the polarization data.

The Planck studies analysed the isotropy violation related to dipolar asymmetry using several methods related to temperature and/or polarization maps. Planck 2015 and 2018 analysis, [6],[9] concluded that the dipole modulation signal is most significant in the lowest multipole window $l \in [2, 64]$ and obtained a dipole modulation amplitude of ~ 0.07 . We will briefly describe some of the methods they used to compute the dipole modulation amplitude.

2.6.1 Bipolar Spherical Harmonics

For a statistically anisotropic field, the CMB 2-point correlation can be expanded in terms of the orthonormal set of bipolar spherical harmonics (BipoSH) basis representation as, [9],[32]

$$C(\hat{n}, \hat{n}') = \sum_{LMl'l'} \tilde{A}_{ll'}^{LM} \{Y_l(\hat{n}) \otimes Y_{l'}(\hat{n}')\}_{LM} \quad 2.16$$

where $A_{ll'}^{LM}$ are the coefficients of the expansion. Also, the BipoSH basis functions, $\{Y_l(\hat{n}) \otimes Y_{l'}(\hat{n}')\}_{LM}$ are tensor products of ordinary spherical harmonic functions.

The coefficients $A_{ll'}^{LM}$ are related to the covariance matrices $\langle a_{lm} a_{l'm'}^* \rangle$ as follows

$$A_{ll'}^{LM} = \sum_{mm'} \langle a_{lm} a_{l'm'}^* \rangle (-1)^{m'} \mathcal{C}_{lml'-m'}^{LM} \quad 2.17$$

where $\mathcal{C}_{lml'-m'}^{LM}$ are Clebsch-Gordan coefficients.

It is convenient to use this basis because it can naturally determine whether the signal is dipolar ($L=1$), quadrapolar ($L=2$) ect. while the power is restricted to specific ranges of angular scales, [9].

In Planck 2015 analysis, [6] they defined a set of BipoSH spectra at every bipolar harmonic moment (L, M) , identified by the index d as follows

$$A_{ll+d}^{LM} = \tilde{A}_{ll+d}^{LM} \frac{\Pi_L}{\Pi_{l(l+d)} \mathcal{C}_{l0(l+d)0}^{L0}} ; (0 \leq d \leq L) \quad 2.18$$

$$\Pi_{l_1 l_2 \dots l_n} = \Pi_{i=n}^n \sqrt{2l_i + 1}$$

where $\mathcal{C}_{l_1 m_1 l_2 m_2}^{LM}$ are the Clebsch-Gordan coefficients. The BipoSH coefficients generalize the CMB power spectra while $A_{ll}^{00} = C_l$ describes the statistically isotropic part of the CMB fluctuations and the other coefficients the anisotropic part, [6]. Thus, it is convenient to use this basis as it can describe all possible violations of statistical anisotropy in a Gaussian CMB sky map.

The following model of the dipole modulation is based on the observational data and has been introduced by [6]

$$T(\hat{n}) = T_0(\hat{n})(1 + M(\hat{n})) \quad 2.19$$

where $T(\hat{n})$ represents the modulated CMB temperature, $T_0(\hat{n})$ is the statistically isotropic random CMB temperature and $M(\hat{n})$ is a dipolar field. The corresponding BipoSH coefficients are written as, [6]

$$A_{ll+1}^{1M} = \bar{A}_{ll+1}^{1M} + m_{1M} G_{ll+1}^1$$

$$G_{ll+1}^1 = \frac{C_l + C_{l+1}}{\sqrt{4\pi}} \sqrt{\frac{(2l+1)(2l+3)}{3}} \mathcal{C}_{l0(l+1)0}^{10} \quad 2.20$$

where \bar{A}_{ll+1}^{1M} corresponds to the BipoSH coefficients to the unknown isotropic CMB field, m_{1M} are the spherical harmonics coefficients of the modulation field and C_l is the best fit angular power spectrum of the CMB.

The power in the dipole modulation field m_1 is written as, [6]

$$m_1 = \frac{1}{3}(|m_{11}|^2 + |m_{10}|^2 + |m_{1-1}|^2) \quad 2.21$$

Also the dipole modulation amplitude is written as, [6]

$$A = 1.5\sqrt{\frac{m_1}{\pi}} \quad 2.22$$

According to [6], the most significant signal is observed in the lowest window $l \in [2, 64]$. Table 2.1 shows the best fit amplitude A and direction corresponding to the dipole modulation as introduced before and to the multipole window $l \in [2, 64]$, for four temperature maps, Commander, NILC, SEVEM, and SMICA. The measured values of the dipole amplitude and direction are consistent for all maps at $A \sim 0.07$.

Method	A	Direction $(l, b)[^\circ]$
Commander	0.067 ± 0.023	$(230, -18) \pm 31$
NILC	0.069 ± 0.022	$(228, -17) \pm 30$
SEVEM	0.067 ± 0.023	$(230, -17) \pm 31$
SMICA	0.069 ± 0.022	$(22, -18) \pm 30$

Table 2.1: Amplitude A and direction of the dipole modulation in Galactic coordinates as estimated for the multipole range $l \in [2, 64]$ using a BipoSH analysis. The Table was adapted by [6].

2.6.2 Dipole modulation: QML analysis

An other estimator to study the level of dipole modulation in the estimates of the CMB sky is the quadratic maximum likelihood (QML) estimator used in both Planck 2015 and 2018 analysis, [6] and [9]. Their results for the temperature amplitude are depicted in Tables 2.2 and 2.3.

2015 TT		
Method	Amplitude	Direction $(l, b)[^\circ]$
Commander	$0.063^{+0.023}_{-0.013}$	$(213, -26) \pm 28$
NILC	$0.064^{+0.027}_{-0.013}$	$(209, -25) \pm 28$
SEVEM	$0.063^{+0.026}_{-0.013}$	$(211, -25) \pm 28$
SMICA	$0.062^{+0.026}_{-0.013}$	$(213, -26) \pm 30$

Table 2.2: Amplitude and direction of the dipole asymmetry signal from the QML analysis for the range $l \in [2 - 64]$, for the 2015 Planck release. The Table was adapted from, [9].

2018 TT		
Method	Amplitude	Direction $(l, b)[^\circ]$
Commander	$0.070^{+0.032}_{-0.015}$	$(221, -22) \pm 31$
NILC	$0.064^{+0.032}_{-0.015}$	$(221, -24) \pm 31$
SEVEM	$0.063^{+0.032}_{-0.015}$	$(221, -22) \pm 31$
SMICA	$0.062^{+0.032}_{-0.015}$	$(221, -22) \pm 31$

Table 2.3: Amplitude and direction of the dipole asymmetry signal from the QML analysis for the range $l \in [2 - 64]$, for the 2018 Planck release. The Table was adapted from, [9].

In the multipole window $l \in [2, 64]$ the polarization data have a very little effect in the dipole modulation amplitude according to Planck 2018 analysis, [9]. More specific, the largest difference is observed when we compare the TT data with the combined TT,TE and EE data for the Commander map, where the dipole amplitude is respectively, $0.070^{+0.032}_{-0.015}$ in the direction $(l = 221^\circ, b = -22^\circ) \pm 31^\circ$ and $0.072^{+0.031}_{-0.015}$ in the direction $(l = 218^\circ, b = -19^\circ) \pm 29^\circ$, Tables 2.3 and 2.4.

2018 TT,TE,EE		
Method	Amplitude	Direction $(l, b)[^\circ]$
Commander	$0.072^{+0.031}_{-0.015}$	$(218, -19) \pm 29$
NILC	$0.069^{+0.032}_{-0.015}$	$(225, -23) \pm 31$
SEVEM	$0.069^{+0.032}_{-0.015}$	$(219, -17) \pm 31$
SMICA	$0.068^{+0.032}_{-0.015}$	$(221, -19) \pm 31$

Table 2.4: The addition of polarization does not have a significant effect on the temperature asymmetry signal for the range $l \in [2 - 64]$. The Table was adapted from, [9].

2.6.3 Variance Asymmetry

An other approach to study the dipolar violations of isotropy is the variance asymmetry, used by both in Planck 2015 and 2018 analysis [6], [6]. The local-variance estimator is a method to study the power asymmetry via the local variance of the CMB fluctuations.

Figure 2.11 depicts the local variance dipole directions for the four temperature maps, Commander, NILC, SEVEM, and SMICA. The image is introduced in the Planck 2018 release, [9]. The preferred directions for the E-mode polarization data are shown in Figure 2.11. As stated in [9] the preferred directions for the E-modes data are relatively close to the corresponding temperature data. Even though the results do not prove the existence of power asymmetry in polarization, they do motivate future observations for the polarization signal.

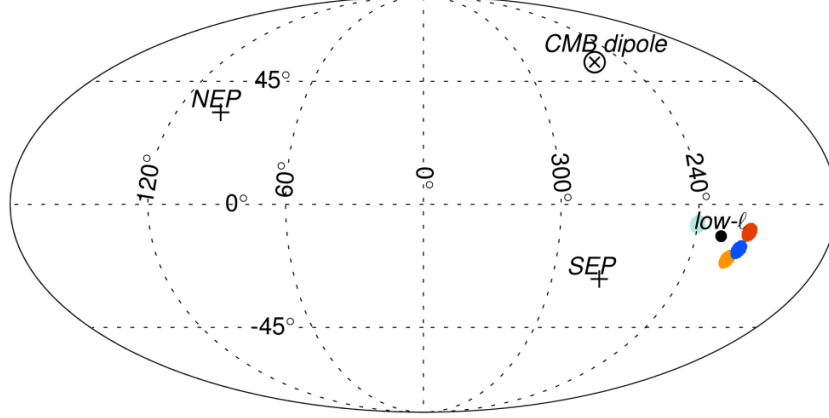


Figure 2.11: E-mode polarization maps for Commander (red), NILC (orange), SEVEM (green), and SMICA (blue). NEP represents the north ecliptic pole, SEP the south and low- l is the preferred dipolar modulation axis as derived from the temperature data. The image is introduced in the Planck 2018 release, [9].

2.7 Cold Spot and Peaks

After the first discovery of the Cold Spot by the WMAP data, [63], Planck 2015 and 2018 data [6],[9] also confirmed its existence. The Cold Spot is centred at Galactic coordinates $(l, b) = (210^\circ, -57^\circ)$. As stated in [63],[49],[17] it is generally accepted that it does not origin from any instrumental systematics or foreground residuals. The Cold Spot might have a physical origin and Planck 2015, [6] summarized several potential physical mechanisms that could explain the origin.

The Planck 2018 polarization data, [9] intended to constrain the physical models that could possibly explain the Cold Spot. For instance, as stated in [6], models which produce secondary anisotropies due to a gravitational effect do not predict any polarization signal.

At the same time, four more peaks were considered as the most anomalous on large angular scales. In total there are two maxima peaks and two minima in the temperature as shown in Figure 2.12, located in southern Galactic hemisphere, [9]. As noted in Planck 2018 analysis, due to correlation between the temperature and E-mode polarization the polarization profile of the peaks should exhibit a particular pattern.

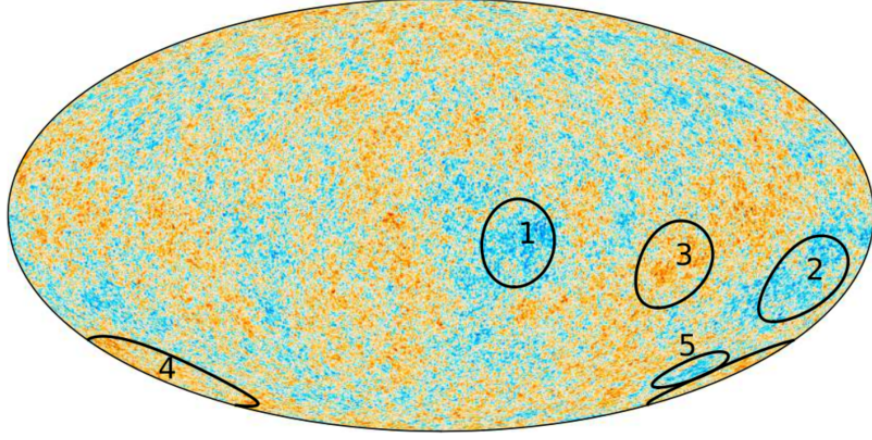


Figure 2.12: The CMB temperature map showing the locations of the large scale peaks. Peak 5 corresponds to the Cold Spot. The picture is adapted from the Planck 2018 mission [9]

The analysis of Planck 2018, [9] concerning the peaks was based on the temperature T and the Stokes parameter Q_r angular profiles. As stated in [9] the presence of a peak would result in larger uncertainties for polarization than for temperature. However the polarization data did not show any signal of the peaks in the covariance of Q_r . Future, more sensitive observations of the polarization field are needed to have a better understanding.

2.8 Point-parity asymmetry

The CMB temperature anisotropy field on the sky, $T(\hat{n})$ can be written with respect to a parity-symmetric $T^+(\hat{n})$ and parity-antisymmetric $T^-(\hat{n})$ functions with respect to the center of the sphere as, [9]

$$T^\pm = \frac{1}{2}[T(\hat{n}) \pm T(-\hat{n})] \quad 2.23$$

where $-\hat{n}$ is the opposite direction of \hat{n} . The functions $T^+(\hat{n})$ and $T^-(\hat{n})$ correspond to spherical harmonics with even and l-modes, respectively.

The Q and U stokes parameters of the polarization field can also be expanded as, [9]

$$\begin{aligned} Q^\pm(\hat{n}) &= \frac{1}{2}[Q(\hat{n}) \pm Q(-\hat{n})] \\ U^\pm(\hat{n}) &= \frac{1}{2}[U(\hat{n}) \mp U(-\hat{n})] \end{aligned} \quad 2.24$$

These functions are described by E and B-mode angular power spectra with even and odd l -modes, respectively. The following estimator of the parity asymmetry has been adopted by the Planck 2015 and 2018 analysis [6], [9]

$$R^{TT}(l_{max}) = \frac{C_+^{TT}(l_{max})}{C_-^{TT}(l_{max})} \quad 2.25$$

where

$$C_{+,-}^{TT} = \frac{1}{l_{tot}^{+,-}} \sum_{l=2, l_{max}}^{+,-} \frac{l(l+1)}{2\pi} C_l^{TT} \quad 2.26$$

where $l_{tot}^{+,-}$ is the total number of even $+$ or odd $-$ multipoles included in the sum up to l_{max} and C^{TT} is the temperature power spectrum.

Since the largest angular scales $0 < l < 30$ correspond to the Sachs-Wolfe plateau of the temperature spectrum, the Universe should not exhibit any parity preference, [9]. However, an odd point-parity preference has been observed in various temperature maps, that is WMAP data releases [46],[44], [31] and confirmed by later Planck studies [6],[9]. If the common mask of Planck 2018 data [9] is applied to Planck 2015 maps they both show a detection of an odd point-parity preference lower-tail probability of about 1% in the multipole range 20 – 30. If the common mask of 2015 data is used to 2018 data then they shows a detection of an odd point-parity preference with a lower tail probability of 0.3% at $l_{max} = 27$, [9]. This lower-tail probability is illustrated in Figure 2.13.

The common mask is defined as the union of the confidence masks from the four SMICA, NILC, SEVEM and COMMANDER maps. Each of the four methods provide a confidence mask to indicate the region of the sky in which the CMB map in temperature and polarization is trusted.

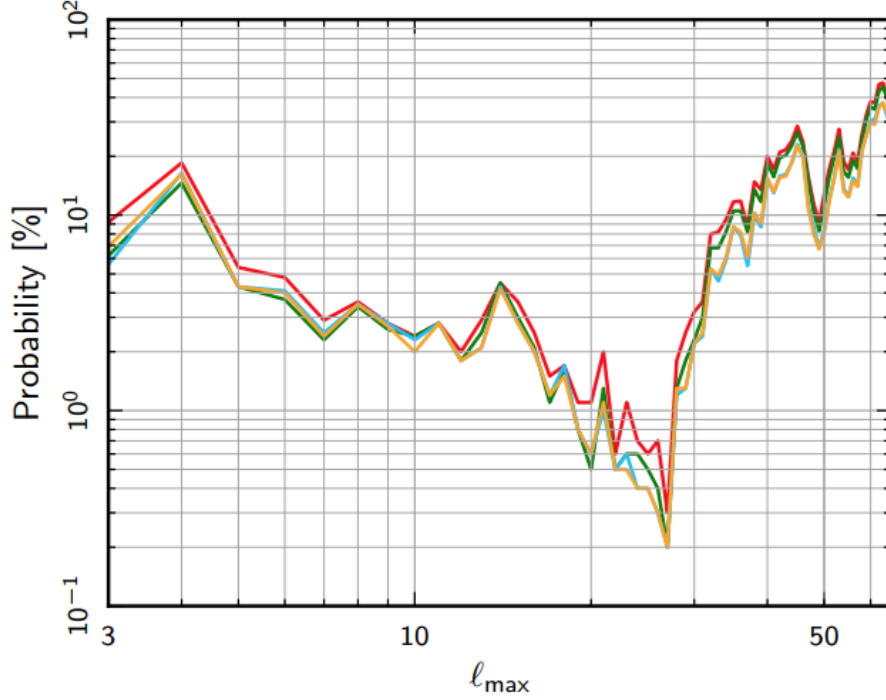


Figure 2.13: Lower-tail probability of the point-parity estimator for Commander (red), NILC (orange), SEVEM, (green), and SMICA (blue). The picture was adopted from the Planck 2015 release [6].

The Planck 2018 data, [9] extended the analysis to look for a point-parity asymmetry in the polarization data. However no such anomalous lower-tail probability has been observed, even though future more sensitive observations are needed to confirm that there is no point-parity asymmetry in polarization.

2.9 Lack of Large Angle Correlations

Planck 2018 Collaboration analysed the polarization data in order to study the lack of correlation in the 2-point angular correlation function at large angular separations, that has been reported previously by several releases such as, [6]. They used the following statistical formalism proposed by [16],

$$S^{XY}(\theta_1, \theta_2) = \int_{\cos\theta_2}^{\cos\theta_1} [\hat{C}_2^{XY}]^2 d(\cos\theta) \quad 2.27$$

where X, Y denote the temperature anisotropy or the Stokes parameters Q_r, U_r . \hat{C}_2^{XY} is an estimate of the corresponding 2-point correlation function. The limits of the separation angle θ_1 and θ_2 are 60° and 180° .

According to Planck 2018 temperature data, [9] there is a lack of correlation on large angular scales. The significance of this results is in agreement with what was previously found. However, the low observed value of the quadrupole might explain the lack of correlation in the temperature maps. For this reason Planck analysis after removing the best fit quadrupole found that there is contribution of the low power in the quadrupole to the lack of large angle correlations.

It has been reported, [16] that we can rule out the possibility that S^{TT} has a small value due to a statistical fluke in the context of a Λ CDM cosmology by measuring the value of S^{TQ} over the angular separation angle $[48^\circ, 120^\circ]$. If this specific value exceeds the limit of $1.403\mu K^4$ then a statistical fluke does not exist, [16]. It was found that the values of S^{TQ} over the angular separation angle $48^\circ, 120^\circ$ are significantly smaller than $1.403\mu K^4$, meaning that the possibility of a statistical fluke still exists.

Chapter 3

The CMB Dipole Modulation

In the following sections, we will examine the possibility that an intrinsic CMB dipole exists due to pre inflationary superhorizon-sized isocurvature fluctuations in scalar fields such as the axion and the ilion, see [22], and contributes together with the kinematic dipole to the CMB temperature anisotropy. In this case, the CMB rest frame does not coincide with the cosmic rest frame of the Hubble flow.

The anisotropies caused by an intrinsic CMB dipole anisotropy and large scale bulk motions are statistically not isotropic at the present day of our particle horizon. At this scale, the angular correlation function $C(\hat{n}, \hat{n}') = \langle \Delta T(\hat{n}) \Delta T(\hat{n}') \rangle$ is not rotationally invariant.

We will examine whether the dipole modulation field observed in [8] can be explained by dipole anisotropies caused not only by our peculiar motions with respect to the CMB but also by superhorizon-sized primordial isocurvature perturbations.

3.1 Kinematic Dipole

We introduce two observers which move relative to each other. The first one corresponds to the CMB rest frame and the second one, to an observer that has a small, finite peculiar velocity relative to the CMB.

The second observer measures for the CMB a black body spectrum and a temperature that depends on the direction of the velocity of the observer as, [60]

$$T(\hat{n}) = T_0 \frac{\sqrt{1-v^2}}{1-v\hat{n} \cdot \hat{v}} \quad 3.1$$

where $\mathbf{v} = v\hat{v}$ is the velocity of the observer with respect to the CMB, T_0 is the average temperature of the CMB corresponding to a homogeneous and an isotropic signal and we have set the speed of light $c = 1$.

We assume that the peculiar velocity of the observer with respect to the CMB

is non relativistic, $v/c \ll 1$. We can expand relation 3.1 in Taylor series as

$$\Delta T(\theta) = T_0(1 + v \cos \theta + (\cos^2 \theta - \frac{1}{2})v^2 + \dots) \quad 3.2$$

where θ is the separation angle between two points in the sky and $\cos \theta = \hat{n} \cdot \hat{v}$. The observer that moves relative to the CMB rest frame with peculiar velocity v , measures a dipole temperature anisotropy due to this peculiar motion described by the following kinematic dipole

$$\frac{\Delta T(\hat{n})}{T_0} = v \hat{n} \cdot \hat{v} \quad 3.3$$

3.2 Superhorizon Perturbations

Inflation explains how a small, smooth patch of the preinflationary Universe evolved to a size that encompasses all that we see today. The current size of preinflationary patch is, [61]

$$\begin{aligned} d_{patch} &= \left(\frac{a_0}{a_{start}} \right) H_I^{-1} \approx e^N \left[\frac{M}{T_{RH}} \right]^{4/3} \left[\frac{T_{RH}}{3K} \right] H_I^{-1} \\ &:= e^{N-N_{min}} H_0^{-1} \end{aligned} \quad 3.4$$

where

$$H_I = \sqrt{\frac{8\pi M^4}{3m_{pl}^2}} \quad 3.5$$

is the Hubble constant during inflation, $H_0 \approx 67.4 km \ s^{-1} Mpc^{-1}$, [57] and $a_0 = 1$ and a_{start} are the scale factors at the present age of the Universe and at the beginning of inflation respectively. M^4 is the vacuum energy that drives inflation and $m_{pl} = 1.22 \cdot 10^{19} GeV$ is the Planck mass. T_{RH} is the temperature to which the Universe is reheated after inflation, [61].

If the number of e-foldings of the the scale factor $N := \ln(a_{end}/a_{start})$ exceeds N_{min} where,

$$N_{min} = 53 + \frac{2}{3} \ln \left(\frac{M}{10^{14} GeV} \right) + \frac{1}{3} \ln \left(\frac{T_{RH}}{10^{10} GeV} \right) \quad 3.6$$

then the Horizon problem is resolved, [61]. Inflation explains the observed homogeneity of causally disconnected regions that exist in the CMB map. If $N > N_{min}$, the preinflationary patch is large enough to encompass the current Hubble volume. Also, the amount of inflation needed to solve the flatness problem, that is why the final density parameter is very close to one, is comparable or less than that required to solve the horizon problem.

If N exceeds N_{min} then scales that were superhorizon sized at the onset of inflation, that is their size was larger than H_I^{-1} their size today is also outside the horizon. Notice that we have consider the speed of light $c = 1$.

A scale that had a physical size of

$$l := e^p H_I^{-1} \quad 3.7$$

at the beginning of inflation where p is some constant, at the present age of the Universe t_0 has a size of, [61]

$$\begin{aligned} L &:= \frac{a_0 l}{a_{start}} = e^P H_0^{-1} \\ P &= p + N - N_{min} \end{aligned} \quad 3.8$$

Notice that the present physical size of the scale L is connected to the current size of the preinflationary Hubble patch as

$$L = e^P d_{patch} \quad 3.9$$

We are interested in scalar perturbations that were superhorizon sized in the beginning of inflation. These scales cannot be affected by events during or after inflation and can provide valuable information about the preinflationary Universe. These superhorizon sized perturbations generate large scale temperature fluctuations in the CMB. Superhorizon sized perturbations can be adiabatic (curvature) or isocurvature, leaving a different imprint in the CMB anisotropies. We are interested in isocurvature perturbations which we will study in Section 3.3. However, before that, we will discuss about adiabatic perturbations.

3.2.1 Adiabatic Perturbations

Adiabatic perturbations correspond to fluctuations in the energy density of the particles taken into consideration. In the model where a scalar field ϕ drives the inflation, quantum fluctuations of the field lead to scale invariant Zeldovich spectrum of adiabatic perturbations, [65], [37].

Grishchuk and Zel'dovich studied superhorizon sized adiabatic perturbations, in an Einstein-de Sitter Universe, [30]. These perturbations lead to temperature anisotropies in the CMB. However, the lowest order term contributing to the anisotropies is quadrupolar, because the intrinsic dipole in the CMB cancels the Doppler dipole induced by our peculiar motion. The same cancellation occurs in a flat Universe containing a cosmological constant Λ , cold dark matter and radiation, as shown in [23].

Adopting the formalism used in [60] the CMB temperature anisotropy using the Sachs-Wolfe effect, [54], in the direction \hat{n} as seen by an observer at spatial position $\mathbf{r} = 0$ is,

$$\frac{\delta T(\hat{n})}{T_0} = \frac{1}{2} \left[\sqrt{R}(\mathbf{x} \cdot \nabla)(\delta_{hor} e^{-i\mathbf{k} \cdot \mathbf{x}}) + \delta_{hor} e^{-i\mathbf{k} \cdot \mathbf{x}} \right]_R^E \quad 3.10$$

where R denotes the reception event at our spatial position $\mathbf{r} = 0$, E denotes the emission event, the scale factor is $R_E \approx (1 + z_E)^{-1} \approx 10^{-3}$ and spatial position $\mathbf{r} = (1 - \sqrt{R_E})\mathbf{x}$, $\mathbf{x} = 2H_0^{-1}\hat{n}$ and $\delta\rho/\rho = (2\pi)^{-3}\delta_k(t)e^{-\mathbf{k} \cdot \mathbf{r}}|_{\mathbf{r}=\mathbf{0}}$.

The first term of 3.10 corresponds to the tilting of the Universe. The density gradient gives us a velocity with respect to the CMB and thus when viewed from the CMB rest frame the Universe appears to be tilted. The second term of 3.10 corresponds to the potential difference between the last-scattering surface and the observer, [60].

In the expansion of the potential term the resulting dipole cancels the Doppler dipole coming from the gradient term, [61], [60]. As a result the dipole of the anisotropy associated with the tilting of the Universe is not observable.

3.3 Intrinsic CMB Dipole

It has been argued [22], [61], [60], that in the inflationary model not only adiabatic perturbations can be generated but also superhorizon sized isocurvature perturbations.

The energy density of the scalar field responsible for the isocurvature fluctuations is negligible comparing to the energy density of the scalar field responsible for the inflation, called the inflaton. Some candidates are the axion field responsible for Peccei-Quinn symmetry breaking and the ilion field, responsible for producing the baryon asymmetry in the model of baryogenesis, [61]. In the following section we will focus on the axion field.

Just like in the inflaton field, quantum fluctuations generate perturbations in the axion field which lead to fluctuations in the local axion-number density. Since the energy density of the axion field is negligible compared to the inflaton these fluctuations do not result in significant curvature fluctuations and this is why they are referred to as isocurvature perturbations. The fluctuations in the number density of axions lead to fluctuations in the temperature of the cosmic microwave background radiation, [61]. The aforementioned are described in detail in [22], [61], [60], [47].

3.3.1 Generation of an Intrinsic Dipole

More specific, the axion field ϕ , is the complex scalar field whose vacuum expectation value $\langle\phi\rangle = f_a e^{i\theta}/\sqrt{2}$ breaks the Peccei-Quinn U(1) symmetry, [12]. Associated with this field the axion, a , is the Nambu-Goldstone boson, corresponding in θ degree of freedom, $a = \theta f_a$. At high temperatures between $T \sim f_a$ and $T \sim 1\text{GeV}$ the axion is massless. After the universe cools down to $T \sim 1\text{GeV}$, QCD instanton effects generate explicit symmetry breaking terms and the axion acquires a small mass, [11].

Since Peccei-Quinn symmetry breaking takes place in a uniform direction the axion field has a uniform value $-\pi < \theta_i < \pi$, which will be in general misaligned with the value $\theta = 0$ where the potential is minimum, $\theta_i \neq 0$. When the axion field acquires mass at $T \sim 1\text{GeV}$ it starts to oscillate around the minimum $\theta = 0$ as a coherent state corresponding to a pressureless cold axion gas.

In de Sitter space all minimally coupled, massless scalar fields have quantum fluctuations. The fluctuations of the axion field ϕ lead to fluctuations in the misalignment angle θ , described as, [61]

$$\frac{\delta\theta}{\theta_0} \approx \frac{H_I}{\pi\theta_0 f_a} \quad 3.11$$

where θ_0 , is the average value of the misalignment angle within the inflationary Hubble patch 3.4.

Since the number density of the axions is proportional to the square of the initial misalignment angle the fluctuations to the local axion-number density are given by

$$\frac{\delta n_a}{n_a} \approx \frac{2\delta\theta}{\theta_0} \quad 3.12$$

Isocurvature perturbations correspond to spatial variations in the equation of state, [61].

Energy cannot be transported on scales larger than the horizon because these regions are casually disconnected. As a result, $\delta\rho = 0$ when the primordial isocurvature fluctuations are superhorizon sized. The isocurvature fluctuations correspond to spatial variations in the equation of state and when the primordial perturbation becomes subhorizon sized the equation of state develops into a density perturbation of similar size. Perturbations in the energy density of the radiation will develop to maintain $\delta\rho = 0$, [61]. Since we follow the work of [61] we assume a two component universe, axions and radiation and neglect the baryons.

When the energy density of the axion is really small compared to the radiation these fluctuations are negligible. As the universe evolves and the temperature drops down to $T \sim 100\text{MeV}$ the axion mass acquires a significant value and the energy density contained in the axion field is no longer negligible, leading to axion density perturbations, [61]. At the same time, metric perturbation arise due to the Sachs-Wolfe effect, 3.10, but this component vanishes as we described previously.

As described in [47] we will make use of the isocurvature initial condition stating that the perturbation in the total energy density is negligible. This means that the perturbations in the energy densities of the of each component adds up to zero, [22]. A CMB temperature anisotropy is generated by the intrinsic fluctuations in the radiation that arise to compensate the axion energy density fluctuation, [61].

$$\delta_T(k) = \frac{-1}{3}\delta_A(k) \quad 3.13$$

here $\delta_T(k) := (\delta T/T)_k$ and $\delta_A(k) := (\delta n_a/n_a)_k = 2\delta\theta_k/\theta_0$.

As we can see, primordial isocurvature fluctuations generate an extra perturbation to CMB temperature. The primordial isocurvature perturbation generate temperature fluctuations associated with the Sachs-Wolfe effect as described in relation 3.10. The dipole component vanishes and the lowest order term is

quadrupolar. Intrinsic fluctuations in the CMB dipole arise to compensate the axion-energy density fluctuation as, [60]

$$\frac{\Delta T(\hat{n})}{T_0} \sim \hat{k} \cdot \hat{n} \left(\frac{H_0^{-1}}{L} \right) \delta_{hor} \quad 3.14$$

where L is the current physical length scale of the fluctuation with wavenumber $\mathbf{k} = k\hat{k}$ and δ_{hor} is the horizon crossing amplitude, that is $\delta_{hor} = (\delta\rho/\rho)_{hor}$ are density perturbations associated with the pre-inflationary fluctuations that existed in the axion-field and depend on the initial conditions, [61].

In conclusion, unlike in a superhorizon-sized adiabatic mode, a primordial isocurvature perturbation will generate CMB temperature anisotropy as described in 3.14 due to the fact that the energy density of radiation, ρ_γ , will develop density perturbations to maintain $\delta\rho_\gamma + \delta\rho_a = 0$.

It is true that for a non SI field, the covariance matrix 2.8 is not diagonal. We will express the power in the dipole modulation field using the amplitudes of the modulation which will then compare it with the Planck 2015 results, [8] in order to constrain the values of the parameters set by the theoretical framework.

3.3.2 Dipole Modulation Amplitude

The dipole modulated CMB anisotropy field in the direction \hat{n} is given by, [56], [9],

$$\Delta T(\hat{n}) = (1 + A\hat{p} \cdot \hat{n})\Delta T^{SI}(\hat{n}) \quad 3.15$$

where $\Delta T(\hat{n}) := T(\hat{n})/T_0 - 1$ and $\Delta T^{SI}(\hat{n})$ is SI CMB temperature anisotropy field. A is the amplitude of the modulation and $\hat{p} := (\theta_p, \phi_p)$ its direction. Relation 3.15 is an analytical representation of the observational data and the origin of the dipole modulation is unknown. We can see that there is a coupling between different harmonics indicating violation of statistical isotropy. The SI temperature field ΔT^{SI} contributes also to the non-SI part of the signal.

The expansion of the modulation field and the dipole direction \hat{p} in to spherical harmonics is written as, [56]

$$A\hat{p} \cdot \hat{n} = \sum_{N=-1}^1 m_{1N} Y_{L=1,N}(\hat{n}) \quad 3.16$$

where m_{1N} ($N = -1, 0, 1$) are the spherical harmonic coefficients of the dipole field. The coefficients m_{11} and m_{1-1} are complex numbers related as, $m_{1-1}^* = m_{11}$.

The modulation amplitude A and the direction (θ_p, ϕ_p) of the modulation dipole are given with respect to the coefficients m_{10} , m_{11}^r (real part of m_{11}), m_{11}^i

(imaginary part of m_{11}), as follows, [56],[6]

$$\begin{aligned} A &= \sqrt{\frac{3}{4\pi}} \sqrt{m_{10}^2 + 2(m_{11}^r)^2 + 2(m_{11}^i)^2} \\ \theta_p &= \cos^{-1} \left[\frac{m_{10}}{A} \sqrt{\frac{3}{4\pi}} \right] \\ \phi_p &= -\tan^{-1} \left[\frac{m_{11}^i}{m_{11}^r} \right] \end{aligned} \tag{3.17}$$

In this work, we will assume that the dipole modulation is related to the intrinsic CMB dipole and to our peculiar motion with respect to the CMB. We express equation 3.15 in terms of the dipole corresponding to our motion 3.3 with respect to the CMB and the dipole corresponding to a superhorizon-sized primordial isocurvature perturbation 3.14 as

$$\Delta T(\hat{n}) = \left[1 + v\hat{n} \cdot \hat{v} + \hat{k} \cdot \hat{n} \left(\frac{H_0^{-1}}{L} \right) \delta_{HOR} \right] \Delta T^{SI}(\hat{n}) \tag{3.18}$$

If we define,

$$\mathbf{p} := v\hat{v} + \frac{H_0^{-1}}{L} \delta_{HOR} \hat{k} \tag{3.19}$$

$$A := \sqrt{v^2 + \left(\frac{H_0^{-1}}{L} \delta_{HOR} \right)^2 + 2v \frac{H_0^{-1}}{L} \delta_{HOR} \cos(\beta)} \tag{3.20}$$

where β is the angle between the observer who moves with velocity $\mathbf{v} = v\hat{v}$ with respect to the CMB and the direction of the superhorizon-sized primordial isocurvature perturbation \hat{k} , then equation 3.18 can be written in the form of 3.15. The vectors \mathbf{p} , \mathbf{k} , \mathbf{v} defined above are depicted in Figure 3.1.

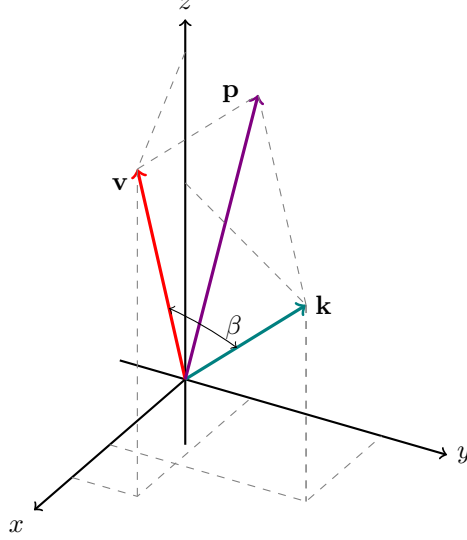


Figure 3.1: An illustration of the vector \mathbf{p} corresponding to the dipole modulation. The vectors \mathbf{v} and \mathbf{k} correspond to the kinematic and the superhorizon-sized dipole, respectively.

We can also define the angle between the direction \hat{n} of the dipole modulated CMB temperature anisotropy field and the direction \hat{p} of the dipole modulation as γ then,

$$\hat{n} \cdot \hat{p} = \cos(\gamma) = \frac{4\pi}{3} \sum_{N=-1}^1 Y_{1N}^*(\hat{p}) Y_{1N}(\hat{n}) \quad 3.21$$

and relation 3.16 becomes,

$$\frac{4\pi}{3} A \sum_{N=-1}^1 Y_{1N}^*(\hat{p}) Y_{1N}(\hat{n}) = \sum_{N=-1}^1 m_{1N} Y_{1N}(\hat{n}) \quad 3.22$$

Using that,

$$\int d\Omega_{\hat{n}} Y_{1N}(\hat{n}) Y_{1N'}^*(\hat{n}) = \delta_{NN'} \quad 3.23$$

we can derive the following expression of the BipoSH coefficients,

$$m_{1N} = \frac{4\pi}{3} A Y_{1N}^*(\hat{p}) \quad 3.24$$

If we expand the temperature anisotropy field as in 3.15 we can express the spherical harmonic coefficients of $\Delta T(\hat{n})$, a_{lm} using 3.16 as, [56]

$$a_{lm} = a_{lm}^{SI} + \sum_{N=-1}^1 m_{1N} \int \Delta T^{SI}(\hat{n}) Y_{L=1,N}(\hat{n}) Y_{lm}^*(\hat{n}) d^2\Omega_{\hat{n}} \quad 3.25$$

where a_{lm}^{SI} are the spherical harmonic coefficients of $\Delta T(\hat{n})^{SI}$. It is worth mentioning that the covariance matrix in spherical harmonic space in a SI CMB sky map is diagonal 2.8, but in the non-SI CMB sky map we consider now, contains off-diagonal terms and can be written as, [56],

$$\begin{aligned} \langle a_{lm} a_{l'm'} \rangle &= C_l \delta_{ll'} \delta_{mm'} \\ &+ \frac{2\sqrt{\pi} \Pi_{ll'}}{3\sqrt{3}} A \sum_{N=-1}^1 Y_{1N}^*(\hat{p}) (C_l (-1)^{l+l'+1} + C_{l'}) C_{l0l'0}^{10} C_{lml'm'}^{1N} \\ &+ \frac{4\pi \Pi_{ll'}}{27} A^2 \sum_{rs} C_r \Pi_r^2 C_{l0r0}^{10} C_{l'0r0}^{10} \sum_{N,N'=-1}^1 Y_{1N}^*(\hat{p}) Y_{1N'}(\hat{p}) C_{lmrs}^{1N} C_{l'm'rs}^{1N'} \end{aligned} \quad 3.26$$

where C_l is the angular power spectrum of a_{lm}^{SI} . Also, $\Pi_{ll'}$ denotes $\sqrt{(2l+1)(2l'+1)}$ and C_{lmrs}^{1N} are the Clebsch-Gordon coefficients.

Following our previous discussion, we would like to derive an expression for the amplitude of the three BipoSH coefficients m_{11}, m_{10} and m_{1-1} . The spherical harmonics used in expression 3.24, $Y_{1N}(\hat{p})$ are the following,

$$Y_{1-1} = \frac{1}{2} \sqrt{\frac{3}{2\pi}} e^{-i\phi_p} \sin\theta_p \quad 3.27$$

$$Y_{10} = \frac{1}{2} \sqrt{\frac{3}{\pi}} \cos\theta_p \quad 3.28$$

$$Y_{11} = -\frac{1}{2} \sqrt{\frac{3}{2\pi}} e^{i\phi_p} \sin\theta_p \quad 3.29$$

where $\hat{p} := (\theta_p, \phi_p)$.

We can write the amplitudes of the BipoSH coefficients as,

$$\begin{aligned} |m_{11}| &= |\sin\theta_p| \sqrt{\frac{2\pi}{3} [v^2 + (\frac{H_0^{-1}}{L} \delta_{HOR})^2 + 2v \frac{H_0^{-1}}{L} \delta_{HOR} \cos(\beta)]} \\ |m_{10}| &= 2 |\cos\theta_p| \sqrt{\frac{\pi}{3} [v^2 + (\frac{H_0^{-1}}{L} \delta_{HOR})^2 + 2v \frac{H_0^{-1}}{L} \delta_{HOR} \cos(\beta)]} \\ |m_{1-1}| &= |\sin\theta_p| \sqrt{\frac{2\pi}{3} [v^2 + (\frac{H_0^{-1}}{L} \delta_{HOR})^2 + 2v \frac{H_0^{-1}}{L} \delta_{HOR} \cos(\beta)]} \end{aligned} \quad 3.30$$

The power in the dipole modulation field is written as in equation 2.21 and the dipole amplitude as in 2.22. Notice that the power in the dipole modulation field depends on the horizon crossing amplitude δ_{hor} , the amplitude of the velocity of the observer v with respect to the CMB rest frame, the angle between the direction of the velocity of the observer, \hat{v} and the direction superhorizon-sized isocurvature mode, \hat{k} as well as the current physical scale of the fluctuation L .

3.4 Parameter Estimation

According to Commander and SEVEM maps¹ considered in [8], the measured value of the dipole amplitude and direction as estimated for the multipole range [2,64] is $A = 0.067 \pm 0.023$ which using expression 2.22 corresponds to a power in the dipole modulation field

$$\frac{m_1}{\pi} \times 10^3 = 1.995 \pm 1.370 \quad 3.31$$

The minimum and maximum value, within the error range, that the power in the dipole modulation field can take are respectively according to 3.31

$$\frac{m_{1,min}}{\pi} \times 10^3 = 0.625 ; \quad \frac{m_{1,max}}{\pi} \times 10^3 = 3.365 \quad 3.32$$

We will study the power in the dipole modulation field as a function of our peculiar velocity v (in km/s), the angle β (in radians), the horizon crossing amplitude δ_{hor} (dimensionless) and the current physical scale of the fluctuation L (in Mpc). Also the power in the dipole modulation in the following discussion will refer to the quantity $m_1/\pi \times 10^3$.

Given relations 2.21 and 3.30 we can write the power in the dipole modulation as

$$\frac{m_1}{\pi} \times 10^3 = 4.4 \times 10^3 \left| v^2 + \left(\frac{H_0^{-1}}{L} \delta_{HOR} \right)^2 + 2v \frac{H_0^{-1}}{L} \delta_{HOR} \cos(\beta) \right| \quad 3.33$$

We see that the right hand side of 3.33 must fall into the range specified in 3.32. In the discussion that follows we will no longer use natural units and the value of the speed of light $c = 299792 km/s$, [57]. The peculiar velocities we consider are between $100 - 400 km/s$, which means that, $4.4 \cdot 10^3 \cdot (v/c)^2 \sim 10^{-3}$ which is negligible compared to the range of values as specified by 3.32.

However it is possible for the remaining terms in 3.33 to have the same order of magnitude as in the range specified by 3.32. More specific, the term $(H_0^{-1}/L)\delta_{hor}$ must be of the order of $\sim 10^{-6} - 10^{-7}$. The size of the physical length L and the horizon crossing amplitude δ_{hor} can vary accordingly. However notice that relations 3.8 and 3.9 set a lower value of the length L . In the following discussion we consider a specific value of the length of the perturbation $L = 4000 \cdot c H_0^{-1}$ and observe how the remaining parameters affect the power in the dipole modulation.

In Figures 3.2, 3.3a and 3.3b we see a representation of the power in the dipole modulation when the horizon crossing amplitude is $\delta_{hor} = 3.48 \cdot 10^{-2}$, $\delta_{hor} = 6.04 \cdot 10^{-2}$ and $\delta_{hor} = 7.72 \cdot 10^{-2}$ respectively. There is a variation of the values that the peculiar velocity and angle β can take, depending on the horizon crossing amplitude. However, δ_{hor} must be of the order of $\sim 10^{-2}$.

¹The NILC and SMICA maps that are also considered in [8], measure a dipole amplitude of $A = 0.069 \pm 0.022$. Since the measured values of the dipole amplitude are consistent for all maps we will consider the Commander and SEVEM maps.

Looking at Figure 3.2, if the power in the dipole modulation as written in 3.32 has a value around its minimum 0.625, then the angle β lies between $\sim 2.5 - 3.8$ radians, while the peculiar velocity lies between $\sim 300 - 400$ km/s. As we move towards to 2.5 and 3.8 radians for an isolevel curve, the peculiar velocity approaches 400 km/s. For example, the middle isolevel curve of Figure 3.2 corresponds to $m_1 \times 10^3 / \pi \sim 0.6199$ and $\beta \sim 3.364 - 2.92$ radians. As we move towards to 3.364 or 2.92 radians the peculiar velocity approaches 400 km/s. The same pattern is observed as the value of the power in the dipole modulation reaches the value ~ 0.66 .

We also notice that as the power in the modulation converges to ~ 0.66 , smaller peculiar velocities are allowed and that the angle β cannot obtain the values $\sim 0 - 1.7$ and $\sim 4.7 - 6.2$ radians. As the power in the dipole modulation increases towards the value 0.71 the corresponding allowed peculiar velocity increases in size while the angle β converges to its extrema 0 and 2π radians. The reflected pattern we observe is due to the $\cos(\beta)$ term in 3.20.

Figures 3.3a and 3.3b represent the peculiar velocity field and the angle β corresponding to a power in the dipole modulation around the value $m_1 / \pi \cdot 10^3 = 1.995$ and $1.92 \cdot 10^{-3}$ (corresponds to the power in the dipole modulation around the maximum), respectively. As before we observe the same pattern with small differences. For a constant value of the power in the dipole modulation between the range of $\sim 1.93 - 1.98$, as the peculiar velocity is decreasing, from 400 km/s to 125 km/s, the angle β converges to π . In the range $\sim 1.98 - 2$, if the peculiar velocity takes a value between 100–125 km/s the angle β varies between $\sim 2 - 4.5$ radians. At the same time as the power in the dipole modulation converges towards to 2.08 the peculiar velocity acquires larger values and the angle β converges to 0 or 2π .

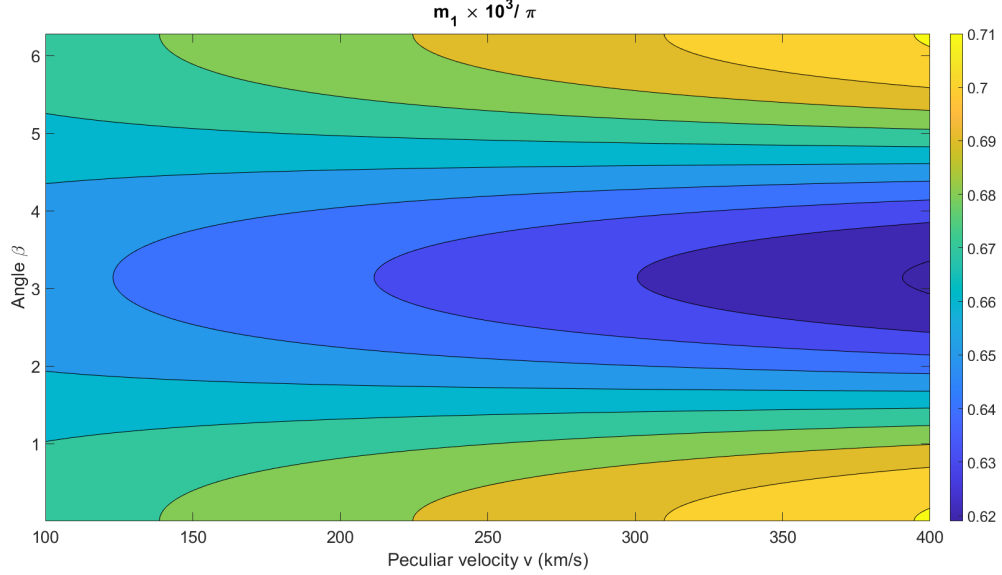


Figure 3.2: The power in the dipole modulation field as a function of the peculiar velocity v (in km/s) and the angle β (in radians) between the direction of the primordial isocurvature temperature anisotropy and the direction of the temperature anisotropy corresponding to the kinematic dipole, for a constant value of the horizon crossing amplitude δ_{hor} . The figure corresponds to the minimum value of the horizon crossing amplitude, $\delta_{hor} = 3.48 \cdot 10^{-2}$ so that the power in the dipole modulation field observed in 3.31 can be explained.

Notice that using equation 3.8 and the fact that we have chosen $L = 4000cH_0^{-1}$, $P \approx 8$. Also, notice that the temperature fluctuations in equation 3.14 are of order of magnitude $(H_0^{-1}/L)\delta_{hor}$. This means, that even though in relation 3.18 we treated equation 3.14 as an exact expression, the order of magnitude of the computed parameters $L, \delta_{hor}, \beta, v$ which interest us, will not change.

Similar patterns as in the above Figures are observed for several combinations of H_0^{-1}/L and δ_{hor} , while $(H_0^{-1}/L) \cdot \delta_{hor} \sim 10^{-6} - 10^{-7}$. According to the above discussion, the origin of the large signal in [8] in the multipole range $2 \leq l \leq 64$, could be explained by the existence of a superhorizon-sized primordial isocurvature perturbation giving rise to a dipole anisotropy intrinsic to the CMB and assuming a temperature anisotropy described by 3.18.

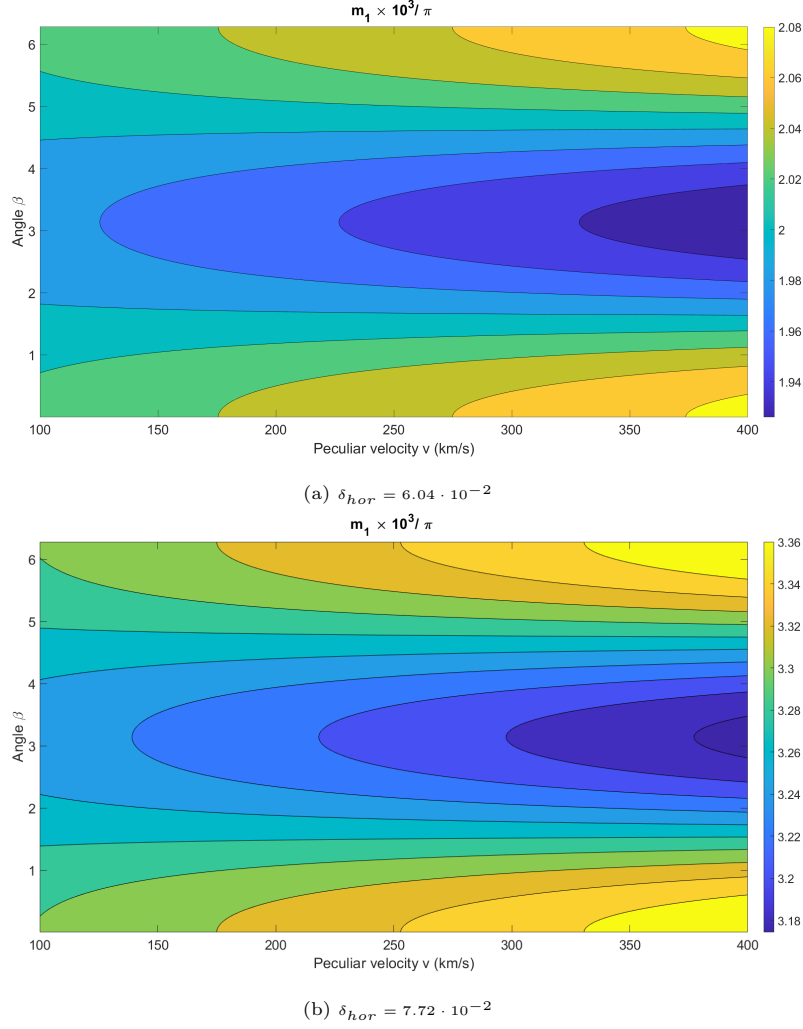


Figure 3.3: The power in the dipole modulation field as a function of the peculiar velocity v (in km/s) and the angle β (in radians) between the direction of the primordial isocurvature temperature anisotropy and the direction of the temperature anisotropy corresponding to the kinematic dipole, for a constant value of the horizon crossing amplitude, $\delta_{hor} = 6.04 \cdot 10^{-2}$ and $\delta_{hor} = 7.72 \cdot 10^{-2}$ in Figure (a) and (b) respectively. Figure (b) corresponds to the maximum value of the horizon crossing amplitude, so that the power in the dipole modulation field observed in 3.31 can be explained.

Chapter 4

Conclusion

In the second Chapter, we described some of the anomalies on the temperature sky map observed by several missions, [63], [6], [9] on large large angular scales. At the same time Planck 2018 [9] search for the equivalent anomalies in the polarization data. However no strong evidence on the existence of these anomalies in the polarization data was found. Concerning the dipolar power asymmetry, an alignment in the proffered direction of the E-mode and temperature dipolar modulation was found but it is unclear if there is a physical mechanism behind it.

Future large-scale and low noise polarization experiments are required to measure the E-modes in order to investigate the anomalies in the polarization maps. At the same time, as depicted in Figure 2.13 there is not a lot information about B-mode polarization. The observation of B-mode polarization in the CMB sky is very important because information about the primordial gravitational waves, emitted during the inflation can be extracted. LiteBIRD, (Lite satellite for the studies of B-mode polarization and Inflation from cosmic background Radiation Detection) is a planned, promising mission that aims to observe the B-mode polarization of the CMB, [41]. It might also be able to test predictions of quantum gravity and those related to the superstring theory, [41]

In the third Chapter, we assumed that we can describe the temperature anisotropy of the CMB as in 3.18, given a kinematic dipole due to our peculiar motion with respect to the CMB and an intrinsic dipole of the CMB coming from a primordial superhorizon-sized isocurvature perturbation of the axion field. We constrained the parameters of our theoretical framework using the observed size of the power in the dipole modulation given by [8]. We observed that the order of magnitude of the horizon crossing amplitude δ_{hor} multiplied by the current physical length of the superhorizon-sized primordial isocurvature perturbation L must be of the order $\sim 10^{-7} - 10^{-6}$. Given this result we can explain the origin of the large signal in [8] in the multipole range $2 \leq l \leq 64$.

However, following [61] we have assumed a two-component Universe (axions and radiation), neglecting any contribution by the baryons. According to [61] isocurvature baryon-number fluctuations can also give rise to temperature anisotropy in the CMB. The local baryon number density is proportional to

the local baryon asymmetry when the baryons and anti-baryons annihilate. In a model of baryogenesis the baryon asymmetry is proportional to the "ilion" field, [15] and thus any misalignment to the ilion field would lead to fluctuations in the local number density of baryons. In a future work, it would be interesting to take into consideration these perturbations, too.

Appendices

Appendix A

SI Condition in Harmonic Space

The condition for statistical isotropy for the two point correlation translates into the following, [33]

$$C(\hat{n}, \hat{n}') = C(\theta), \quad ; \quad \theta = \cos^{-1}(\hat{n} \cdot \hat{n}') \quad \text{A.1}$$

where θ is the separation angle between two points in the sky. We can expand it in terms of Legendre polynomials

$$C(\theta) = \frac{1}{4\pi} \sum_{l=2}^{\infty} (2l+1) C_l P_l(\cos\theta) \quad \text{A.2}$$

where

$$P(\hat{n} \cdot \hat{n}') = \frac{4\pi}{2l+1} \sum_{m=-l}^l Y_{lm}^*(\hat{n}) Y_{lm}(\hat{n}') \quad \text{A.3}$$

Substituting the expression 2.5 for the spherical harmonic coefficients a_{lm} in the covariance matrix 2.8 and expressing it in terms of two point correlation we get, [33]

$$\begin{aligned} \langle a_{lm} a_{l'm'}^* \rangle &= \int \int d\Omega_{\hat{n}} d\Omega_{\hat{n}'} Y_{lm}(\hat{n}) Y_{l'm'}(\hat{n}') \langle \Delta T(\hat{n}) \Delta T(\hat{n}') \rangle \\ &= \int \int d\Omega_{\hat{n}} d\Omega_{\hat{n}'} Y_{lm}(\hat{n}) Y_{l'm'}(\hat{n}') C(\hat{n}, \hat{n}') \end{aligned} \quad \text{A.4}$$

Substituting the spherical harmonic expansion of Legendre polynomials into the relation A.2 the expression for the covariant matrix becomes

$$\begin{aligned} \langle a_{lm} a_{l'm'}^* \rangle &= \int \int d\Omega_{\hat{n}} d\Omega_{\hat{n}'} Y_{lm}(\hat{n}) Y_{l'm'}(\hat{n}') \sum_{l_1} C_{l_1} \sum_{m_1} Y_{l_1 m_1}(\hat{n}) Y_{l_1 m_1}(\hat{n}') \\ &= \sum_{l_1} C_{l_1} \sum_{m_1} \delta_{ll_1} \delta_{l'l_1} \delta_{mm_1} \delta_{m'm_1} \\ &= C_l \delta_{ll'} \delta_{mm'} \end{aligned} \quad \text{A.5}$$

where we have used the orthonormality relation of spherical harmonics

$$\int d\Omega_{\hat{n}} Y_{lm}(\hat{n}) Y_{l'm'}^*(\hat{n}) = \delta_{ll'} \delta_{mm'} \quad \text{A.6}$$

Bibliography

- [1] ESA and the Planck Collaboration. Power spectrum of temperature fluctuations in the cosmic microwave background, 2013. https://sci.esa.int/documents/34222/35279/1567216755608-Planck_power_spectrum_625.jpg.
- [2] ESA and the Planck Collaboration. Cosmic microwave background polarisation amplitude filtered to show scales around 5 degrees and larger, 2019. <https://sci.esa.int/web/planck/-/61398-the-cmb-polarisation-on-large-angular-scales>.
- [3] ESA and the Planck Collaboration. Cosmic microwave background temperature fluctuations filtered to show scales around 5 degrees and larger, 2019. <https://sci.esa.int/web/planck/-/61397-the-cmb-temperature-on-large-angular-scales>.
- [4] Wayne Hu. Eb modes. <http://background.uchicago.edu/~whu/animbut/anim6.html>.
- [5] P. A. R. Ade, N. Aghanim, Y. Akrami, P. K. Aluri, M. Arnaud, M. Ashdown, J. Aumont, C. Baccigalupi, A. J. Banday, and et al. Planck 2015 results. *Astronomy & Astrophysics*, 594:A16, Sep 2016.
- [6] P. A. R. Ade, N. Aghanim, Y. Akrami, P. K. Aluri, M. Arnaud, M. Ashdown, J. Aumont, C. Baccigalupi, A. J. Banday, and et al. Planck2015 results. *Astronomy & Astrophysics*, 594:A16, Sep 2016.
- [7] P. A. R. Ade, N. Aghanim, C. Armitage-Caplan, M. Arnaud, M. Ashdown, F. Atrio-Barandela, J. Aumont, C. Baccigalupi, A. J. Banday, and et al. Planck2013 results. xxiii. isotropy and statistics of the cmb. *A & A*, 571:A23, Oct 2014.
- [8] P. A. R. Ade, N. Aghanim, M. Arnaud, M. Ashdown, J. Aumont, C. Baccigalupi, A. J. Banday, R. B. Barreiro, J. G. Bartlett, and et al. Planck 2015 results - xiii. cosmological parameters. *Astronomy & Astrophysics*, 594:A13, Sep 2016.
- [9] Y. Akrami et al. Planck 2018 results. VII. Isotropy and Statistics of the CMB. 6 2019.

- [10] Y. Akrami, Y. Fantaye, A. Shafieloo, H. K. Eriksen, F. K. Hansen, A. J. Banday, and K. M. Górski. Power asymmetry in wmap and planck temperature sky maps as measured by a local variance estimator. *The Astrophysical Journal*, 784(2):L42, Mar 2014.
- [11] M. Axenides, R. Brandenberger, and M. Turner. Minosaxenidesrobertbrandenbergmichaelturner. *Physics Letters B*, 126:178–182, 06 1983.
- [12] Minos Axenides, Robert Brandenberger, and Michael Turner. Development of axion perturbations in an axion dominated universe. *Physics Letters B*, 126(3-4):178–182, June 1983.
- [13] José Luis Bernal, Licia Verde, and Adam G. Riess. The trouble with H0. *Journal of Cosmology and Astroparticle Physics*, 2016(10):019–019, 10 2016.
- [14] Juan C. Bueno Sánchez. The inflationary origin of the cold spot anomaly. *Physics Letters B*, 739:269–278, Dec 2014.
- [15] A.G. Cohen, D.B. Kaplan, and A.E. Nelson. Spontaneous baryogenesis at the weak phase transition. *Physics Letters B*, 263(1):86 – 92, 1991.
- [16] Craig J. Copi, Dragan Huterer, Dominik J. Schwarz, and Glenn D. Starkman. Large-angle cosmic microwave background suppression and polarization predictions. *Monthly Notices of the Royal Astronomical Society*, 434(4):3590–3596, Aug 2013.
- [17] M. Cruz, M. Tucci, E. Martínez-González, and P. Vielva. The non-gaussian cold spot in wilkinson-microwave-anisotropy-probe: significance, morphology and foreground contribution. *Monthly Notices of the Royal Astronomical Society*, 369(1):57–67, May 2006.
- [18] M. Cruz, N. Turok, P. Vielva, E. Martinez-Gonzalez, and M. Hobson. A cosmic microwave background feature consistent with a cosmic texture. *Science*, 318(5856):1612–1614, Dec 2007.
- [19] Andrei Cuceu, James Farr, Pablo Lemos, and Andreu Font-Ribera. Baryon acoustic oscillations and the hubble constant: past, present and future. *Journal of Cosmology and Astroparticle Physics*, 2019(10):044–044, Oct 2019.
- [20] Bartłomiej Czech, Matthew Kleban, Klaus Larjo, Thomas S Levi, and Kris Sigurdson. Polarizing bubble collisions. *Journal of Cosmology and Astroparticle Physics*, 2010(12):023–023, Dec 2010.
- [21] Sudeep Das, Tobias Marriage, Peter Ade, Paula Aguirre, M. Amiri, John Appel, L. Barrientos, Elia Battistelli, John Bond, Ben Brown, Biogeelina Burger, Jay Chervenak, Mark Devlin, Simon Dicker, W. Doriese, Joanna Dunkley, Rolando Dunner, T. Essinger-Hileman, Ryan Fisher, and and Zhao. The atacama cosmology telescope: A measurement of the cosmic

- microwave background power spectrum at 148 and 218 ghz from the 2008 southern survey. *The Astrophysical Journal*, 729:62, 02 2011.
- [22] G. Efstathiou and J. R. Bond. Isocurvature cold dark matter fluctuations. *Monthly Notices of the Royal Astronomical Society*, 218(1):103–121, 01 1986.
- [23] Adrienne L. Erickcek, Sean M. Carroll, and Marc Kamionkowski. Super-horizon perturbations and the cosmic microwave background. *Physical Review D*, 78(8), Oct 2008.
- [24] H. K. Eriksen, A. J. Banday, K. M. Gorski, and P. B. Lilje. The n-point correlation functions of the first-year wilkinson microwave anisotropy probe sky maps. *The Astrophysical Journal*, 622(1):58–71, Mar 2005.
- [25] H. K. Eriksen, F. K. Hansen, A. J. Banday, K. M. Gorski, and P. B. Lilje. Asymmetries in the cosmic microwave background anisotropy field. *The Astrophysical Journal*, 605(1):14–20, 04 2004.
- [26] ESA and the Planck Collaboration. A compilation of recent cmb angular power spectrum measurements from which cosmological inferences are drawn, 2018. <https://www.cosmos.esa.int/web/planck/picture-gallery>.
- [27] Stephen M. Feeney, Matthew C. Johnson, Daniel J. Mortlock, and Hiranya V. Peiris. First observational tests of eternal inflation. *Physical Review Letters*, 107(7), Aug 2011.
- [28] F. Finelli, J. García-Bellido, A. Kovács, F. Paci, and I. Szapudi. Supervoids in the wise-2mass catalogue imprinting cold spots in the cosmic microwave background. *Monthly Notices of the Royal Astronomical Society*, 455(2):1246–1256, Nov 2015.
- [29] C. Gordon, W. Hu, D. Huterer, and T. Crawford. Spontaneous isotropy breaking: A mechanism for cmb multipole alignments. *Physical Review D*, 72, 10 2005.
- [30] L. P. Grishchuk and Ia. B. Zeldovich. Long-wavelength perturbations of a friedmann universe, and anisotropy of the microwave background radiation. *Soviet Astronomy*, 22:125–129, April 1978.
- [31] A. Gruppuso, F. Finelli, P. Natoli, F. Paci, P. Cabella, A. De Rosa, and N. Mandolesi. New constraints on parity symmetry from a re-analysis of the wmap-7 low-resolution power spectra. *Monthly Notices of the Royal Astronomical Society*, 411(3):1445–1452, Nov 2010.
- [32] Amir Hajian and Tarun Souradeep. Measuring the statistical isotropy of the cosmic microwave background anisotropy. *The Astrophysical Journal*, 597(1):L5–L8, Oct 2003.

- [33] Amir Hajian and Tarun Souradeep. The cosmic microwave background bipolar power spectrum: Basic formalism and applications, 2004.
- [34] Amir Hajian and Tarun Souradeep. Testing global isotropy of three-year wilkinson microwave anisotropy probe (wmap) data: Temperature analysis. *Phys. Rev. D*, 74:123521, Dec 2006.
- [35] F. K. Hansen, A. J. Banday, K. M. Górski, H. K. Eriksen, and P. B. Lilje. 704(2):1448–1458, oct 2009.
- [36] F. K. Hansen, A. J. Banday, and K. M. Górski. Testing the cosmological principle of isotropy: local power-spectrum estimates of the wmap data. *Monthly Notices of the Royal Astronomical Society*, 354(3):641–665, 11 2004.
- [37] E. R. Harrison. Fluctuations at the threshold of classical cosmology. *Phys. Rev. D*, 1:2726–2730, May 1970.
- [38] J. Hoftuft, H. K. Eriksen, A. J. Banday, K. M. Górski, F. K. Hansen, and P. B. Lilje. INCREASING EVIDENCE FOR HEMISPHERICAL POWER ASYMMETRY IN THE FIVE-YEARWMAPDATA. *The Astrophysical Journal*, 699(2):985–989, 06 2009.
- [39] Wayne Hu and Martin White. A cmb polarization primer. *New Astronomy*, 2(4):323–344, Oct 1997.
- [40] Kaiki Taro Inoue and Joseph Silk. Local voids as the origin of large-angle cosmic microwave background anomalies. i. *The Astrophysical Journal*, 648(1):23–30, Sep 2006.
- [41] JAXA. Litebird (lite satellite for the studies of b-mode polarization and inflation from cosmic background radiation detection). <http://www.litebird-europe.eu>, note = Accessed: 24/07/2020.
- [42] Joshua A. Kable, Graeme E. Addison, and Charles L. Bennett. Quantifying the cmb degeneracy between the matter density and hubble constant in current experiments. *The Astrophysical Journal*, 871(1):77, jan 2019.
- [43] Jean Kaplan, Jacques Delabrouille, Pablo Fosalba, and Cyrille Rosset. Cmb polarization as complementary information to anisotropies. *Comptes Rendus Physique*, 4(8):917–924, Oct 2003.
- [44] Jaiseung Kim and Pavel Naselsky. ANOMALOUS PARITY ASYMMETRY OF THE WILKINSON MICROWAVE ANISOTROPY PROBE POWER SPECTRUM DATA AT LOW MULTIPOLES. *The Astrophysical Journal*, 714(2):L265–L267, apr 2010.
- [45] Arthur Kosowsky. Introduction to microwave background polarization. *New Astronomy Reviews*, 43(2-4):157–168, Jul 1999.

- [46] Kate Land and João Magueijo. Is the universe odd? *Physical Review D*, 72(10), Nov 2005.
- [47] Andrew R. Liddle and David H. Lyth. The cold dark matter density perturbation. *Physics Reports*, 231(1-2):1–105, Aug 1993.
- [48] Yen-Ting Lin and Benjamin D. Wandelt. A beginner’s guide to the theory of cmb temperature and polarization power spectra in the line-of-sight formalism. *Astroparticle Physics*, 25(2):151–166, Mar 2006.
- [49] Xin Liu and Shuang Nan Zhang. Non-gaussianity due to possible residual foreground signals in wilkinson microwave anistropy probe first year data using spherical wavelet approaches. *The Astrophysical Journal*, 633(2):542–551, Nov 2005.
- [50] J. D. McEwen, S. M. Feeney, M. C. Johnson, and H. V. Peiris. Optimal filters for detecting cosmic bubble collisions. *Physical Review D*, 85(10), May 2012.
- [51] Polarization of the Cosmic Microwave Background Radiation. Yasin memari, March 2007. The Royal Observatory, Edinburgh.
- [52] Adam G. Riess, Lucas M. Macri, Samantha L. Hoffmann, Dan Scolnic, Stefano Casertano, Alexei V. Filippenko, Brad E. Tucker, Mark J. Reid, David O. Jones, Jeffrey M. Silverman, and et al. A 2.4 *The Astrophysical Journal*, 826(1):56, Jul 2016.
- [53] Lawrence Rudnick, Shea Brown, and Liliya R. Williams. Extragalactic radio sources and thewmapcold spot. *The Astrophysical Journal*, 671(1):40–44, Dec 2007.
- [54] R. K. Sachs and A. M. Wolfe. Perturbations of a Cosmological Model and Angular Variations of the Microwave Background. *Astrophysical Journal*, 147:73, January 1967.
- [55] Dominik J Schwarz, Craig J Copi, Dragan Huterer, and Glenn D Starkman. Cmb anomalies after planck. *Classical and Quantum Gravity*, 33(18):184001, Aug 2016.
- [56] S. Shaikh, S. Mukherjee, S. Das, B. D. Wandelt, and T. Souradeep. Joint bayesian analysis of large angular scale CMB temperature anomalies. *Journal of Cosmology and Astroparticle Physics*, 2019(08):007–007, 08 2019.
- [57] M. Tanabashi, K. Hagiwara, K. Hikasa, K. Nakamura, Y. Sumino, F. Takahashi, J. Tanaka, K. Agashe, G. Aielli, C. Amsler, M. Antonelli, D. M. Asner, H. Baer, Sw. Banerjee, R. M. Barnett, T. Basaglia, C. W. Bauer, J. J. Beatty, V. I. Belousov, J. Beringer, S. Bethke, A. Bettini, H. Bichsel, O. Biebel, K. M. Black, E. Blucher, O. Buchmuller, V. Burkert, M. A. Bychkov, R. N. Cahn, M. Carena, A. Ceccucci, A. Cerri, D. Chakraborty, M.-C. Chen, R. S. Chivukula, G. Cowan, O. Dahl, G. D’Ambrosio, T. Damour,

- D. de Florian, A. de Gouvêa, T. DeGrand, P. de Jong, G. Dissertori, B. A. Dobrescu, M. D’Onofrio, M. Doser, M. Drees, H. K. Dreiner, D. A. Dwyer, P. Eerola, S. Eidelman, J. Ellis, J. Erler, V. V. Ezhela, W. Fetscher, B. D. Fields, R. Firestone, B. Foster, A. Freitas, H. Gallagher, L. Garren, H.-J. Gerber, G. Gerbier, T. Gershon, Y. Gershtein, T. Gherghetta, A. A. Godizov, M. Goodman, C. Grab, A. V. Gritsan, C. Grojean, D. E. Groom, M. Grünewald, A. Gurtu, T. Gutsche, H. E. Haber, C. Hanhart, S. Hashimoto, Y. Hayato, K. G. Hayes, A. Hebecker, S. Heinemeyer, B. Heltsley, J. J. Hernández-Rey, J. Hisano, A. Höcker, J. Holder, A. Holtkamp, T. Hyodo, K. D. Irwin, K. F. Johnson, M. Kado, M. Karliner, U. F. Katz, S. R. Klein, E. Klempt, R. V. Kowalewski, F. Krauss, M. Kreps, B. Krusche, Yu. V. Kuyanov, Y. Kwon, O. Lahav, J. Laiho, J. Lesgourgues, A. Liddle, Z. Ligeti, C.-J. Lin, C. Lippmann, T. M. Liss, L. Littenberg, K. S. Lugovsky, S. B. Lugovsky, A. Lusiani, Y. Makida, F. Maltoni, T. Mannel, A. V. Manohar, W. J. Marciano, A. D. Martin, A. Masoni, J. Matthews, U.-G. Meißner, D. Milstead, R. E. Mitchell, K. Mönig, P. Molaro, F. Moortgat, M. Moskovic, H. Murayama, M. Narain, P. Nason, S. Navas, M. Neubert, P. Nevski, Y. Nir, K. A. Olive, S. Pagan Griso, J. Parsons, C. Patrignani, J. A. Peacock, M. Pennington, S. T. Petcov, V. A. Petrov, E. Pianori, A. Piepke, A. Pomarol, A. Quadt, J. Rademacker, G. Raffelt, B. N. Ratcliff, P. Richardson, A. Ringwald, S. Roesler, S. Rolli, A. Romaniouk, L. J. Rosenberg, J. L. Rosner, G. Rybka, R. A. Ryutin, C. T. Sachrajda, Y. Sakai, G. P. Salam, S. Sarkar, F. Sauli, O. Schneider, K. Scholberg, A. J. Schwartz, D. Scott, V. Sharma, S. R. Sharpe, T. Shutt, M. Silari, T. Sjöstrand, P. Skands, T. Skwarnicki, J. G. Smith, G. F. Smoot, S. Spanier, H. Spieler, C. Spiering, A. Stahl, S. L. Stone, T. Sumiyoshi, M. J. Syphers, K. Terashi, J. Terning, U. Thoma, R. S. Thorne, L. Tiator, M. Titov, N. P. Tkachenko, N. A. Törnqvist, D. R. Tovey, G. Valencia, R. Van de Water, N. Varelas, G. Venanzoni, L. Verde, M. G. Vincter, P. Vogel, A. Vogt, S. P. Wakely, W. Walkowiak, C. W. Walter, D. Wands, D. R. Ward, M. O. Wascko, G. Weiglein, D. H. Weinberg, E. J. Weinberg, M. White, L. R. Wiencke, S. Willocq, C. G. Wohl, J. Womersley, C. L. Woody, R. L. Workman, W.-M. Yao, G. P. Zeller, O. V. Zenin, R.-Y. Zhu, S.-L. Zhu, F. Zimmermann, P. A. Zyla, J. Anderson, L. Fuller, V. S. Lugovsky, and P. Schaffner. Review of particle physics. *Phys. Rev. D*, 98:030001, Aug 2018.
- [58] Kenji Tomita. Second-order gravitational effects of local inhomogeneities on cmb anisotropies and non-gaussian signatures. *Physical Review D*, 72, 09 2005.
- [59] Kenji Tomita and Kaiki Taro Inoue. Second order gravitational effects on cmb temperature anisotropy in λ dominated flat universes. *Physical Review D*, 77(10), May 2008.
- [60] M. S. Turner. The tilted universe. *General Relativity and Gravitation*, 24(1):1–7, 01 1992.

-
- [61] Michael S. Turner. Tilted universe and other remnants of the preinflationary universe. *Phys. Rev. D*, 44:3737–3748, Dec 1991.
 - [62] Eleonora Di Valentino, Alessandro Melchiorri, and Joseph Silk. Cosmic discordance: Planck and luminosity distance data exclude lcdm, 2020.
 - [63] P. Vielva, E. Martinez-Gonzalez, R. B. Barreiro, J. L. Sanz, and L. Cayon. Detection of non-gaussianity in the wilkinson microwave anisotropy probe first-year data using spherical wavelets. *The Astrophysical Journal*, 609(1):22–34, Jul 2004.
 - [64] Matias Zaldarriaga. The polarization of the cosmic microwave background, 2003.
 - [65] Ya.B. Zeldovich. Gravitational instability: An approximate theory for large density perturbations. *Astron. Astrophys.*, 5:84–89, 1970.